



# A variational phase-field framework for thermal softening and dynamic ductile fracture

David E. Torres <sup>a</sup>, Tianchen Hu <sup>b</sup>, Andrew J. Stershic <sup>c</sup>, Timothy R. Shelton <sup>c</sup>, John E. Dolbow <sup>a,\*</sup>

<sup>a</sup> Duke University, United States of America

<sup>b</sup> Currently at Argonne National Laboratory, United States of America

<sup>c</sup> Sandia National Laboratories, United States of America

## ARTICLE INFO

**Keywords:**  
Plasticity  
Phase-field  
Shear  
Shear-band  
Variational

## ABSTRACT

A variational phase field model for dynamic ductile fracture is presented. The model is designed for elasto-viscoplastic materials subjected to rapid deformations in which the effects of heat generation and material softening are dominant. The variational framework allows for the consistent inclusion of plastic dissipation in the heat equation as well as thermal softening. It employs a coalescence function to degrade fracture energy during regimes of high plastic flow. A variationally consistent form of the Johnson-Cook model is developed for use with the framework. Results from various benchmark problems in dynamic ductile fracture are presented to demonstrate capabilities. In particular, the ability of the model to regularize shear band formation and subsequent damage evolution in two- and three-dimensional problems is demonstrated. Importantly, these phenomena are naturally captured through the underlying physics without the need for phenomenological criteria such as stability thresholds for the onset of shear band formation.

## 1. Introduction

The phase-field method for fracture has proven to be flexible and has been applied to a wide range of fields. Extensions to shear band applications have been made in recent years [1,2] and have demonstrated the ability of the phase-field model to work in tandem with shear failure phenomenon. In this work, we apply a fully variational phase-field model for ductile fracture to simulate mesh-insensitive shear band formation. The variational model is a continuation of that described by Hu et al. [3], which is an extension of foundational work done by Francfort and Marigo [4] and Bourdin et al. [5]. The model postulates ductile fracture as a minimization problem and incorporates plastic energy and dissipation in a thermodynamically consistent manner. This results in a model and accompanying simulations that are capable of representing shear-band initiation and propagation, followed by fracture, in a mesh-insensitive manner and without the need for any ad-hoc criteria.

Shear band failure has been intensively studied in recent decades [1,6,7]. Shear banding is described as a failure mechanism in which a thin region of a ductile material catastrophically collapses under high deformations. Shear bands are characterized by very large strains, whereas the surrounding regions remain relatively unperturbed. Thus, shear bands are considered a strain localization phenomenon. Shear banding has been documented experimentally in various materials, such as geomaterials [8] and metal alloys [9]. This work focuses on high-strength metals under high-speed loading conditions. Shear failure in high-strength metals is found in applications where high-speed impacts are common, such as ballistics [10] and high-speed machining [11].

\* Corresponding author.

E-mail address: [jdolbow@duke.edu](mailto:jdolbow@duke.edu) (J.E. Dolbow).

A shear band represents a localization instability in a system [12,13]. In any spatially discrete setting, such as that used with finite elements, measures must be taken to ensure that the width of simulated shear bands is not mesh dependent [12,14]. Several methods exist to address this issue, such as the use of gradient plasticity [15,16], higher-order continuum models [17], viscous regularization [18], and through the incorporation of additional physics [19]. In particular, the work of Batra and Kim [19] points to the utility of incorporating thermal diffusion to achieve shear band regularization. Across a range of viscoplastic models, their work demonstrated how heat conduction can play a significant role in governing the width of the shear band. Additionally, Wright and Batra [20] observed the existence of separate length scales for visco-plastic and thermal effects. The recent work of Jacquey et al. [13] quantified, through stability analysis, the influence of inertial effects, viscous effects, and thermal coupling on the regularization of a shear band in both space and time. Their work explores the conditions under which strain localization is regularized using rate-dependent plasticity and describes the separate length scales associated with viscosity, inertial effects, and heat conduction.

Although phase-field regularizations of fracture were originally developed for brittle materials, several models have since been advanced for ductile materials [2,3,21,22]. Additional challenges arise when introducing rate dependence and plastic dissipation. The combination of rate dependence and plastic dissipation through heat generation leads to shear failure, an additional failure mode to account for, leading to research on phase-field damage coupled with shear failure. The work of Arriaga and Waisman [1] utilized stability analysis to predict the order in which the damage and momentum equation system becomes unstable under different circumstances as a tool to predict the dominant failure mode in a system. The work of Miehe et al. [2] utilized von Mises gradient thermoplasticity, in which the plastic flow was terminated at fracture onset. This model was used to simulate a brittle-to-ductile transition, which is where loading conditions influence the formation of brittle or ductile fractures. The work of Wang et al. [22] utilized a variational phase-field model to simulate shear band formation. Their work explicitly tied the width of the shear band to the regularized width of the damage field, effectively neglecting its ability to vary temporally and spatially.

This work adapts the framework described in Hu et al. [3] for coupled plasticity and damage by creating a variationally-consistent thermo-mechanical-fracture model through the inclusion of heat generation due to plastic dissipation. The framework is flexible and allows for the inclusion of a range of plastic flow rules and hardening laws. Here, plasticity is represented with  $J_2$  plasticity and the Johnson–Cook hardening law [23]. Additionally, the model utilizes a linear crack geometric function, known as the AT-1 functional, proposed by Ambrosio and Tortorelli [24] such that damage nucleation is governed by an energetic threshold. The model described in this work can capture shear failure before the initiation of phase-field damage through plastic dissipation and temperature-dependent material degradation via the Johnson–Cook hardening law. When the spatial fields are sufficiently resolved, the model captures shear band formation without any spurious mesh sensitivity. The viscous terms introduced by the rate-dependent Johnson–Cook hardening law regularize the strain localization in time while the gradient term in the heat equation regularizes the shear band in space. Through the governing equations, the model therefore incorporates physically-consistent length scales in both time and space. By including these effects, the model displays shear band regularization without ad-hoc parameters, all within a fully variational framework. This is in contrast to previous efforts investigating coupled shear-banding and fracture, such as the work by McAuliffe and Waisman [25], that are not variationally consistent.

The paper is organized as follows. Section 2 lays out the theoretical framework, integrating thermal effects, plastic dissipation, and fracture mechanics. It includes details of the variational form of the Johnson–Cook model, the objective function, and the discretization in space and time. Results from various numerical simulations are then provided in Section 3. This includes simple problems illustrating the constitutive behavior, as well as two- and three-dimensional simulations of coupled shear band formation and fracture. Finally, a summary and some concluding remarks are provided in Section 4.

## 2. Theory

Let  $\phi(X, t)$  denote the deformation map at time  $t$ , mapping a material point  $X \in \Omega$  to a point in the current configuration  $x \in \phi(\Omega, t)$ . The deformation gradient is defined as  $F = \partial x / \partial X$  and  $J = \det(F)$  is the associated Jacobian. A multiplicative decomposition of the deformation gradient  $F = F^e F^p$ , is adopted for plasticity. Following the work of Hu et al. [3] and Yang et al. [26], the state of the system is characterized by the set of variables  $S = \{\phi, F^p, \bar{\epsilon}^p, d, \nabla d, T\}$ , where  $\bar{\epsilon}^p$  is the effective plastic strain,  $d$  is the damage variable, and  $T$  is the temperature. Here and in what follows, the symbol  $\nabla$  denotes the gradient operator with respect to the reference coordinates  $X \in \Omega$ .

Furthermore, a set of generalized velocities are defined,  $\mathcal{V} = \{\dot{\phi}, \dot{F}^p, \dot{\bar{\epsilon}}^p, \dot{d}\}$ . The total energy  $\Psi(S)$  of the system is given by

$$\Psi(S) = W^e(F, F^p, d) + W^p(\bar{\epsilon}^p, d, T) + F(d, \nabla d), \quad (1)$$

where  $W^e(F, F^p, d)$  is the strain energy,  $W^p(\bar{\epsilon}^p, d, T)$  is the plastic energy, and  $F(d, \nabla d)$  is the fracture energy. We write  $\psi$ ,  $w^e$ ,  $w^p$ , and  $f$  for the accompanying volumetric densities in the reference configuration. The corresponding dual kinetic potential is defined as:

$$H(\mathcal{V}, S) = W^{p*}(\dot{\bar{\epsilon}}^p, S) + \Lambda(d, S), \quad (2)$$

where  $W^{p*}(\dot{\bar{\epsilon}}^p, S)$  is the viscoplastic dissipation,  $\Lambda(d, S)$  is the fracture dissipation. In what follows,  $\pi$ ,  $w^{p*}$ , and  $\lambda$  are used to denote the accompanying volumetric densities in the reference configuration.

Furthermore, we introduce the following bulk dissipation inequality:

$$\int_{\Omega} [\dot{u}(S, \dot{s}) + \dot{k}(\dot{\phi}) + \pi(\mathcal{V}, S) - T \dot{s} - \chi(g)] \, dV - P(\mathcal{V}) \geq 0, \quad (3)$$

where  $\dot{s}$  is the rate of entropy,  $\dot{u}$  is the rate of change of the internal energy,  $\dot{k}$  is the rate of change in the kinetic energy,  $P$  is the external power expenditure,  $\mathbf{g} = -\frac{1}{T}\nabla T$  is the normalized temperature gradient, and  $\chi(\mathbf{g}) = \frac{\kappa}{2}\mathbf{g} \cdot \mathbf{g}$  is the Fourier potential with thermal conductivity  $\kappa$ . The potential  $\chi(\mathbf{g})$  can be related to the heat flux  $\mathbf{h}$  with  $-\mathbf{h} = \chi_{,\mathbf{g}} = -\kappa\nabla T$ . Through this, the following Lagrangian is defined:

$$L(A, \dot{s}, T) = \int_{\Omega} [\rho_0 \mathbf{a} \cdot \dot{\mathbf{a}} + \psi(S) + \pi(\mathcal{V}, S) - T\dot{s} - \chi(\mathbf{g})] \, dV - P(\mathcal{V}), \quad (4)$$

where  $\mathbf{a}$  is the acceleration and  $\rho_0$  is the reference density. The initial boundary value problem is governed by the inf-sup condition,

$$(\mathcal{V}, \dot{s}, T) = \arg \left[ \inf_{\mathcal{V}, \dot{s}} \sup_T L(A, \dot{s}, T) \right], \quad (5)$$

involving the infimum of the sum of the rate of the total energy and its viscous counterpart, along with the supremum of the temperature. These conditions are subject to constraints specified in Section 2.2. The work of Yang et al. [26] shows that taking the supremum of  $T$  recovers the heat equation.

Finally, the mass balance and angular momentum balance are given by

$$J\rho = \rho_0, \quad \forall X \in \Omega, \quad (6)$$

$$\mathbf{F}\mathbf{F}^T = \mathbf{F}\mathbf{P}^T, \quad \forall X \in \Omega, \quad (7)$$

where  $\rho$  specifies the density in the current configuration and  $\mathbf{P}$  is the first Piola–Kirchhoff stress.

## 2.1. Constitutive choices

This work uses the Hencky hyperelastic model with a volumetric-deviatoric decomposition, as described in Hu et al. [3]. The plastic energy  $W^p(\bar{\epsilon}^p, d, T)$  is assumed to take a form that is consistent with  $J_2$  plasticity with a rate-dependent Johnson–Cook hardening law. The fracture energy  $F(d, \nabla d)$  is based on a regularized model of fracture with a finite critical fracture strength.

Mechanical-fracture coupling is modeled using a degradation function,  $g(d)$ . The elastic energy based on the Hencky hyperelastic model with a volumetric-deviatoric split is given by

$$W^e(\mathbf{C}, \mathbf{C}^p, d) = \int_{\Omega} w^e(\mathbf{C}, \mathbf{C}^p, d) \, dV = \int_{\Omega} g(d)w_{(A)}^e(\mathbf{C}, \mathbf{C}^p) + w_{(I)}^e(\mathbf{C}) \, dV, \quad (8a)$$

$$w_{(A)}^e(\mathbf{C}^e) = \frac{1}{2}K \langle \text{tr}(\boldsymbol{\epsilon}^e) \rangle_+^2 + G \text{dev} \boldsymbol{\epsilon}^e : \text{dev} \boldsymbol{\epsilon}^e, \quad (8b)$$

$$w_{(I)}^e(\mathbf{C}^e) = \frac{1}{2}K \langle \text{tr}(\boldsymbol{\epsilon}^e) \rangle_-^2, \quad (8c)$$

where  $K$  is the bulk modulus,  $G$  is the shear modulus,  $\mathbf{C} = \mathbf{F}^T \mathbf{F}$  is the right Cauchy–Green strain tensor,  $\mathbf{C}^e = \mathbf{F}^{eT} \mathbf{F}^e$  is the elastic right Cauchy–Green strain tensor,  $\boldsymbol{\epsilon}^e = \frac{1}{2}\ln(\mathbf{C}^e)$  is the logarithmic elastic strain, and  $\langle \cdot \rangle_{\pm}$  denotes the signed version of the Macaulay bracket. In the above,  $w_{(A)}^e$  and  $w_{(I)}^e$  denote the active and inactive portions of the elastic energy, respectively, and  $\text{dev}$  is the deviator. In keeping with standard assumptions for phase-field models of fracture, only the active portion of the elastic energy is degraded with the degradation function  $g(d)$ .

The plastic energy is assumed to take the form

$$W^p(\bar{\epsilon}^p, d) = \int_{\Omega} w^p(\bar{\epsilon}^p, d) \, dV, \quad (9a)$$

$$w^p(\bar{\epsilon}^p, d) = g(d) \left[ (1 - Q) \left( A\bar{\epsilon}^p + B\epsilon_0^p \left( \frac{\bar{\epsilon}^p}{\epsilon_0^p} \right)^{n+1} \frac{1}{n+1} \right) \right] S(T), \quad (9b)$$

with the accompanying viscoplastic dissipation of the form,

$$W^{p*}(\bar{\epsilon}^p, \dot{\bar{\epsilon}}^p, d) = \int_{\Omega} w^{p*}(\bar{\epsilon}^p, \dot{\bar{\epsilon}}^p, d) \, dV, \quad (10a)$$

$$w^{p*}(\bar{\epsilon}^p, \dot{\bar{\epsilon}}^p, d) = g(d) \dot{\bar{\epsilon}}^p \left[ Q \left( A + B \left( \frac{\bar{\epsilon}^p}{\epsilon_0^p} \right)^n \right) + \left( A + B \left( \frac{\bar{\epsilon}^p}{\epsilon_0^p} \right)^n \right) \left( C \ln \frac{\dot{\bar{\epsilon}}^p}{\dot{\bar{\epsilon}}_0^p} - C \right) \right] S(T), \quad (10b)$$

$$S(T) = 1 - \left( \frac{T - T_0}{T_m - T_0} \right)^m, \quad (10c)$$

where  $A$  is the reference yield stress,  $B$  is the strain hardening modulus,  $C$  is the strain rate sensitivity,  $n$  is the strain exponent,  $m$  is the temperature exponent,  $\epsilon_0^p$  is the reference plastic strain,  $\dot{\bar{\epsilon}}_0^p$  is the reference plastic strain rate,  $T_0$  is the reference temperature,  $T_m$  is the melting temperature,  $Q$  is the Taylor–Quinney factor, and  $S(T)$  is a thermal softening function. Eqs. (9b) and (10b) represent a variational form of the Johnson–Cook model [27], split into energetic and dissipative energies, designed so that  $w_{,\bar{\epsilon}^p}^p + w_{,\dot{\bar{\epsilon}}^p}^{p*}$  recovers the standard result for the yield stress  $\sigma_y$ , namely

$$\sigma_y = \left[ A + B \left( \frac{\bar{\epsilon}^p}{\epsilon_0^p} \right)^n \right] \left( 1 + C \ln \frac{\dot{\bar{\epsilon}}^p}{\dot{\bar{\epsilon}}_0^p} \right) S(T), \quad (11)$$

when  $g(d) = 1$ . Note that both the elastic  $W^e$  and plastic  $W^p$  energies utilize the same degradation function  $g(d)$ . Other works have introduced separate degradation functions for the elastic and plastic energetic contributions; however, in this work, a common degradation function is used for both.

The fracture potential is represented using a standard phase-field approximation in terms of the fracture toughness  $\mathcal{G}_c$  and the damage regularization length  $l$ . This takes the form

$$F(d, \nabla d; l) = \int_{\Omega} f(d, \nabla d; l) \, dV = \int_{\Omega} \mathcal{G}_c \gamma(d, \nabla d; l) \, dV, \quad (12a)$$

$$\gamma(d, \nabla d; l) = \frac{1}{c_0 l} (\alpha(d) + l^2 \nabla d \cdot \nabla d), \quad (12b)$$

$$c_0 = 4 \int_0^1 \sqrt{\alpha(d)} \, dd, \quad (12c)$$

where  $\gamma$  is the crack surface density function,  $\alpha$  is the crack geometric function, and  $c_0$  is a normalization constant.

In this work, we utilize the AT-1 model [24], wherein

$$\alpha(d) = d, \quad (13)$$

$$c_0 = \frac{8}{3}. \quad (14)$$

The following simple quadratic degradation function is employed,

$$g(d) = (1 - d)^2(1 - \eta) + \eta, \quad (15)$$

where  $\eta$  is a (small) residual degradation that remains when the damage approaches one. The fracture dissipation is defined as

$$\Lambda(\dot{d}, \bar{\epsilon}^p; c_1, c_2, c_3) = \int_{\Omega} \lambda(\dot{d}, \bar{\epsilon}^p; c_1, c_2, c_3) \, dV, \quad (16)$$

$$\lambda(\dot{d}, \bar{\epsilon}^p; c_1, c_2, c_3) = g_c(\bar{\epsilon}^p; c_1, c_2, c_3) \frac{\mathcal{G}_c}{c_0 l} \alpha_d(d) \dot{d}, \quad (17)$$

where  $g_c$  is a coalescence function (defined in Section 2.2). The choices of degradation function and selection of an AT-1 model leads to a critical fracture energy,

$$\psi_c g_c(\bar{\epsilon}^p; c_1, c_2, c_3) = \frac{3}{16} \frac{\mathcal{G}_c}{l}, \quad (18)$$

that must be exceeded by the fracture-driving energy (defined in Section 2.2) in order for any damage to develop. Finally, the external power expenditure is given by

$$P(\mathcal{V}) = \int_{\Omega} p_b \, dV + \int_{\partial\Omega_t} p_t \, dA + \int_{\partial\Omega_c} p_c \, dA - \int_{\Omega} p_s \, dV, \quad (19a)$$

$$p_b(\dot{\phi}) = \rho_0 \mathbf{b} \cdot \dot{\phi}, \quad (19b)$$

$$p_t(\dot{\phi}) = t \cdot \dot{\phi}, \quad (19c)$$

$$p_c(T) = h_c \left[ T - T_{\infty} \ln \frac{T}{T_0} \right], \quad (19d)$$

$$p_s(T) = \rho_0 q \ln \left( \frac{T}{T_0} \right), \quad (19e)$$

where  $\mathbf{b}$  is the referential body force per unit mass,  $t$  is the traction force acting on the Neumann boundary,  $h_c$  is the heat transfer coefficient,  $T_{\infty}$  is the far-field temperature, and  $q$  is the heat source. We note that (19d) corresponds to a convective boundary condition.

## 2.2. Lagrangian

Following Yang et al. [26] we introduce the concept of an equilibrium temperature,

$$T^{eq} = \frac{du(S, \dot{s})}{ds}. \quad (20)$$

where  $u(S, \dot{s})$  is the internal energy of the system and  $s$  is the entropy.  $T^{eq}$  represents the temperature state when there is no net exchange of thermal energy between the system and its surroundings. Consequently,  $T^{eq}$  is a state function as it reflects the internal thermodynamic state of the system. Additionally, a dummy integration factor  $T/T^{eq}$  is introduced. The temperature,  $T$ , is treated as an external temperature, meaning it is an imposed condition rather than one based on internal conditions. We act with the assumption that, at equilibrium, the external temperature is equal to the equilibrium temperature:

$$T^{eq} - T = 0. \quad (21)$$

This assumption lends itself to the coupling of thermal and mechanical processes, such as thermal softening and plastic dissipation, as these mechanisms are directly tied to the internal state of the system through the equilibrium temperature. Importantly, the

equilibrium temperature allows for the objective function to represent both the conservation of momentum and energy in a way that satisfies the second law of thermodynamics. Further details can be found in the work of Yang et al. [26]. The equilibrium temperature allows (2) to be recast as,

$$\Pi(\mathcal{V}, \mathcal{S}) = W^{p*} \left( \frac{T}{T^{\text{eq}}} \dot{\bar{\varepsilon}}^p, \mathcal{S} \right) + \Lambda(d, \mathcal{S}), \quad (22)$$

and (4) to be recast as,

$$L(A, \dot{s}, T) = \int_{\Omega} [\rho_0 \mathbf{a} \cdot \dot{\phi} + \psi(\mathcal{S}) + \pi(\mathcal{V}, \mathcal{S}) + (T^{\text{eq}} - T) \dot{s} - \chi(g)] \, dV - P(\mathcal{V}). \quad (23)$$

The postulated potential is fully defined using a set of hyperparameters  $\mathcal{H} = \{l, C, c_1, c_2, c_3, \eta\}$  and material constants  $\mathcal{M} = \{K, G, \epsilon_0^p, \dot{\epsilon}_0^p, A, B, C, m, n, \mathcal{G}_c\}$  defined on a geometry  $\Omega$ . In what follows, the explicit dependence on  $\mathcal{H}$  and  $\mathcal{M}$  are dropped for readability. By substituting (8a), (9b), (10b), and (12) into  $\psi(\mathcal{S})$  and  $\pi(\mathcal{V}, \mathcal{S})$  in (23), the Lagrangian is obtained:

$$\begin{aligned} L = & \int_{\Omega} \rho_0 \dot{\phi} \cdot \mathbf{a} \, dV + \int_{\Omega} w_{,\mathbf{F}}^e(\mathbf{F}, \mathbf{F}^p, d) : \dot{\mathbf{F}} \, dV + \int_{\Omega} w_{,\mathbf{F}^p}^e(\mathbf{F}, \mathbf{F}^p, d) : \dot{\mathbf{F}}^p \, dV + \int_{\Omega} w_{,d}^e(\mathbf{F}, \mathbf{F}^p, d) \dot{d} \, dV \\ & + \int_{\Omega} w_{,\dot{\bar{\varepsilon}}^p}^p(\bar{\varepsilon}^p, \dot{\bar{\varepsilon}}^p, d) \dot{\bar{\varepsilon}}^p \, dV + \int_{\Omega} w_{,d}^p(\mathbf{F}, \mathbf{F}^p, d, T) \dot{d} \, dV \\ & + \int_{\Omega} f_{,d}(d, \nabla d) \dot{d} \, dV + \int_{\Omega} f_{,\nabla d}(d, \nabla d) \nabla \dot{d} \, dV \\ & + \int_{\Omega} w^{p*}(\bar{\varepsilon}^p, \frac{T}{T^{\text{eq}}} \dot{\bar{\varepsilon}}^p, d, T) \, dV + \int_{\Omega} \lambda(\dot{d}, \bar{\varepsilon}^p) \, dV \\ & + \int_{\Omega} (T^{\text{eq}} - T) \dot{s} \, dV - \int_{\Omega} \chi(g) \, dV \\ & - \int_{\Omega} p_b(\dot{\phi}) \, dV - \int_{\partial\Omega_l} p_t(\dot{\phi}) \, dA - \int_{\partial\Omega_c} p_c(T) \, dA + \int_{\Omega} p_s(T) \, dV. \end{aligned} \quad (24)$$

The local state variables,  $\dot{\mathbf{F}}^p, \dot{\bar{\varepsilon}}^p, \dot{s}$ , are separated from the global state variables,  $\dot{\phi}, \dot{d}$ , as they can be updated point-wise. Hence we reorganize (5) as,

$$(\mathcal{V}, \dot{s}, T) = \arg \left\{ \inf_{\dot{\phi}, \dot{d}} \sup_T L \left[ \inf_{\dot{\mathbf{F}}^p, \dot{\bar{\varepsilon}}^p, \dot{s}} \psi(\mathcal{S}) - T \dot{s} - \chi(g) + \pi(\mathcal{V}, \mathcal{S}) \right] \right\}. \quad (25)$$

Then the minimization of  $\mathbf{F}^p$  and  $\bar{\varepsilon}^p$  can be defined as

$$(\dot{\mathbf{F}}^p, \dot{\bar{\varepsilon}}^p) = \arg \left\{ \inf_{\mathbf{F}^p, \dot{\bar{\varepsilon}}^p} \left[ w_{,\mathbf{F}^p}^e(\mathbf{F}, \mathbf{F}^p, d) : \mathbf{F}^p + w_{,\dot{\bar{\varepsilon}}^p}^p(\bar{\varepsilon}^p, \dot{\bar{\varepsilon}}^p, d) \dot{\bar{\varepsilon}}^p + w^{p*}(\bar{\varepsilon}^p, \frac{T}{T^{\text{eq}}} \dot{\bar{\varepsilon}}^p, d, T) \right] \right\}, \quad (26)$$

subject to flow rule constraints, which are defined below. For (25) and (26) minimization is performed with respect to the generalized velocity,  $\mathcal{V}$ , along with the following constraints:

$$\mathcal{V} = \arg \min_{\mathcal{V}} \dot{\Psi}(\mathcal{V}) + \Pi(\mathcal{V}, \mathcal{S}) - P(\mathcal{V}), \quad (27a)$$

subject to,

$$\dot{\bar{\varepsilon}}^p \geq 0, \quad (27b)$$

$$\dot{d} \geq 0, \quad (27c)$$

$$\text{tr}(\dot{\mathbf{F}}^p \mathbf{F}^{p-1}) = 0, \quad (27d)$$

$$\|\dot{\mathbf{F}}^p \mathbf{F}^{p-1}\|^2 - \frac{3}{2} |\dot{\bar{\varepsilon}}^p|^2 = 0, \quad (27e)$$

where (27b) enforces plastic irreversibility, (27c) enforces damage irreversibility, (27d) ensures that all plastic flow is isochoric as defined by  $J_2$  plasticity, and (27e) is the Prandtl-Reuss flow rule.

The variation of (25) with respect to  $\dot{\phi}$  leads to the governing equations for the balance of linear momentum<sup>1</sup>

$$\nabla \cdot \mathbf{P} + \rho_0 \mathbf{b} = \rho_0 \mathbf{a}, \quad \forall \mathbf{X} \in \Omega, \quad (28a)$$

$$\mathbf{P} \cdot \mathbf{n}_0 = t, \quad \forall \mathbf{X} \in \partial\Omega_l, \quad (28b)$$

where  $\mathbf{n}_0$  denotes the unit outward normal in the reference configuration. The first Piola-Kirchhoff stress  $\mathbf{P}$  is given by

$$\mathbf{P} = w_{,\mathbf{F}}^e(\mathbf{F}, \mathbf{F}^p, d) = \boldsymbol{\tau} \mathbf{F}^{-T}, \quad (29a)$$

$$\boldsymbol{\tau} = g(d) \boldsymbol{\tau}_{(A)} + \boldsymbol{\tau}_{(I)}, \quad (29b)$$

$$\boldsymbol{\tau}_{(A)} = K \langle \text{tr}(\boldsymbol{\varepsilon}^e) \rangle_+ \mathbf{I} + 2G \text{dev} \boldsymbol{\varepsilon}^e, \quad (29c)$$

$$\boldsymbol{\tau}_{(I)} = K \langle \text{tr}(\boldsymbol{\varepsilon}^e) \rangle_- \mathbf{I}, \quad (29d)$$

<sup>1</sup> This derivation and the constitutive equations that are adopted are consistent with the Coleman-Noll procedure. For additional details, see [26,28].

where  $\tau$  is the Kirchhoff stress.

Taking the variation of (26) with respect to  $\dot{\mathbf{F}}^p$  and  $\dot{\bar{\varepsilon}}^p$ , subject to the constraints (27b), (27d), (27e) results in the equations for plasticity. The Prandtl-Reuss flow rule is recovered:

$$\dot{\mathbf{F}}^p \mathbf{F}^{p-1} = \dot{\bar{\varepsilon}}^p \mathbf{N}^p, \quad (30a)$$

$$\mathbf{N}^p = \sqrt{\frac{3}{2}} \frac{\text{dev}(\mathbf{M})}{\|\text{dev}(\mathbf{M})\|}, \quad (30b)$$

where  $\mathbf{M} = -w_{,\mathbf{F}^p}^e \mathbf{P}^T$  is the Mandel stress and  $\mathbf{N}^p$  is the flow direction. Considering the polar decomposition  $\mathbf{F}^e = \mathbf{R}^e \mathbf{U}^e$ , it can also be shown that  $\mathbf{M} = \mathbf{R}^{eT} \boldsymbol{\tau} \mathbf{R}^e$  and  $\|\mathbf{M}\| = \|\boldsymbol{\tau}\|$  (see Hu et al. [3]). From this, acting with the assumption that  $\mathbf{R}^e \approx \mathbf{I}$  for most ductile metals,  $\mathbf{N}^p$  can be approximated as

$$\mathbf{N}^p \approx \sqrt{\frac{3}{2}} \frac{\text{dev}(\boldsymbol{\tau})}{\|\text{dev}(\boldsymbol{\tau})\|}. \quad (31)$$

The Karush–Kuhn–Tucker (KKT) system for plasticity is also recovered:

$$\phi^p \leq 0, \quad (32a)$$

$$\dot{\bar{\varepsilon}}^p \geq 0, \quad (32b)$$

$$\phi^p \dot{\bar{\varepsilon}}^p = 0, \quad (32c)$$

where  $\phi^p$  is the yield surface (applying  $\mathbf{M} \approx \boldsymbol{\tau}$ )

$$\begin{aligned} \phi^p &= \|\text{dev}(\boldsymbol{\tau})\| - \sqrt{\frac{2}{3}} \left( w_{,\bar{\varepsilon}^p}^p (\bar{\varepsilon}^p, d) + w_{,\dot{\bar{\varepsilon}}^p}^{p*} (\bar{\varepsilon}^p, \dot{\bar{\varepsilon}}^p, d) \right), \\ &= \|\text{dev}(\boldsymbol{\tau})\| - S(T) \sqrt{\frac{2}{3}} g(d) \left[ (1 - Q) \left( A + B \left( \frac{\bar{\varepsilon}^p}{\varepsilon_0^p} \right)^n \right) \right. \\ &\quad \left. + \left( A + B \left( \frac{\bar{\varepsilon}^p}{\varepsilon_0^p} \right)^n \right) \left( Q + C \ln \frac{\dot{\bar{\varepsilon}}^p}{\varepsilon_0^p} \right) \right]. \end{aligned} \quad (33)$$

Taking a variation of (25) with respect to  $T$  and using  $T \dot{s} = \frac{\dot{T}}{T} \rho_0 c_v$ , as defined by Matsurbara and Terada [29], the heat equation with convective boundary condition is recovered

$$\begin{aligned} \rho_0 c_v \dot{T} &= -\nabla \cdot \mathbf{h} + \delta_i + \delta_t, \quad \forall \mathbf{X} \in \Omega, \\ \mathbf{h} \cdot \mathbf{n}_0 &= h_c(T - T_\infty), \quad \forall \mathbf{X} \in \partial\Omega_c, \end{aligned} \quad (34)$$

where  $c_v$  is the specific heat,  $\delta_i$  is the internal dissipation density, and  $\delta_t$  represents the dissipation density accounting for thermal effects in the thermodynamic conjugate. For clarity, we note that the boundary condition for external heat convection results from taking a variation with respect to temperature  $T$ , and as such presents differently from that of (19d).

The dissipation densities are defined as

$$\begin{aligned} \delta_i &= g(d) w_{,\dot{\bar{\varepsilon}}^p}^{p*} \dot{\bar{\varepsilon}}^p, \\ &= g(d) J(T) \dot{\bar{\varepsilon}}^p \left( A + B \left( \frac{\bar{\varepsilon}^p}{\varepsilon_0^p} \right)^n \right) \left( Q + C \ln \frac{\dot{\bar{\varepsilon}}^p}{\varepsilon_0^p} \right), \end{aligned} \quad (35a)$$

$$\begin{aligned} \delta_t &= g(d) T \frac{\partial w_{,\dot{\bar{\varepsilon}}^p}^p}{\partial T} \dot{\bar{\varepsilon}}^p, \\ &= g(d) T \left( -m \frac{(T-T_0)^{m-1}}{(T_m-T_0)^m} \right) (1 - Q) \left( A + B \left( \frac{\bar{\varepsilon}^p}{\varepsilon_0^p} \right)^n \right). \end{aligned} \quad (35b)$$

The variation of (25) with respect to  $d$  results in the governing equations for damage:

$$-\phi^f = -\nabla \cdot \left( \frac{2G_c l}{c_0} \nabla d \right) + \widehat{\mathcal{G}_c} \alpha_d(d) + \Xi(\mathbf{F}, \mathbf{F}^p, \bar{\varepsilon}^p, d), \quad (36a)$$

$$\Xi = g_{,d}(d) w_{,\langle A \rangle}^e(\mathbf{F}, \mathbf{F}^p) + g_{,d}(d) w^p(\bar{\varepsilon}^p, T), \quad (36b)$$

$$\widehat{\mathcal{G}_c}/\mathcal{G}_c = g_c(\bar{\varepsilon}^p) = \frac{1 - c_2}{e^{(\bar{\varepsilon}^p - c_1)/c_3} + 1} + c_2, \quad (36c)$$

where  $\phi^f$  is the failure surface,  $\Xi(\mathbf{F}, \mathbf{F}^p, \bar{\varepsilon}^p, d)$  is the generalized fracture driving energy,  $\widehat{\mathcal{G}_c}$  is the modified fracture toughness, and  $\mathcal{G}_c$  is the unmodified fracture toughness. The coalescence function represents the weakening of the fracture toughness brought about by the material defects associated with plastic strain, such as void nucleation.

The form of the driving energy above departs from the work of Hu et al. [3] in several significant ways due to the relative importance of plastic energy in dynamics (with thermal softening) compared to quasi-statics. We direct the reader to the detailed discussion in Hu et al. [30] of two different classes of phase-field for ductile fracture models, namely Elastic-Plastic-Damage (EPD) and Elastic-Plastic-Plastic Damage (EPPD). In an EPD formulation, only the elastic energy contributes to the generalized fracture

driving energy  $\Xi$ . In a variational framework, this results when the plastic energy is not degraded with the damage through  $g(d)$ . By comparison, in an EPPD model, both the elastic and plastic energies contribute to the generalized fracture driving energy  $\Xi$ .

Hu et al. [3] adopted an EPD model to reproduce the results of problems in ductile, quasi-static fracture. When used with an energetic decomposition for the elastic energy, a model can be constructed wherein crack growth does not occur under compression. Importantly, for the class of problems examined in Hu et al. [30], the magnitude of the plastic energy was comparable to that of the elastic energy at the onset of failure. In contrast, in the dynamic thermo-mechanical problems examined in this work, the plastic energy in the shear band can be several orders of magnitude larger than the elastic energy. In essence, the problems are dominated by plasticity. In such settings, the use of the elastic energy alone to drive damage evolution was simply found to be insufficient. Accordingly, this work adopts an EPPD formulation, as indicated by the expression for  $\Xi$ , above.

In a similar vein, the functional form of the coalescence dissipation function introduces a constitutive choice that diverges from the approach proposed by Hu et al. [30], wherein the critical fracture energy was degraded by a  $g_c$  that exponentially decayed with the effective plastic strain  $\bar{\epsilon}^p$ . By contrast, the above construction of  $g_c$  introduces a sharp drop in the critical fracture energy once  $\bar{\epsilon}^p$  approaches the material constant  $c_1$ . This shift was found to be necessary in order to delay the degradation of  $G_c$  until the plastic strain was sufficiently large. In essence, this further facilitates the representation of damage nucleation after shear band formation.

### 2.3. Discretization

The initial boundary-value problem is described as the following:

#### The initial boundary-value problem

linear momentum balance: $\nabla \cdot \mathbf{P} + \rho_0 \mathbf{b} = \rho_0 \mathbf{a}$ ,	$\forall \mathbf{X} \in \Omega$ ,
$\mathbf{P} \cdot \mathbf{n}_0 = \mathbf{t}$ ,	$\forall \mathbf{X} \in \partial\Omega_t$ ,
$\mathbf{u} = \mathbf{u}_g$ ,	$\forall \mathbf{X} \in \partial\Omega_u$ ,
stress-transformation relation: $\mathbf{P} = \boldsymbol{\tau} \mathbf{F}^{-T}$ ,	$\forall \mathbf{X} \in \Omega$ ,
heat transfer: $\rho_0 c_v \dot{T} = -\nabla \cdot \mathbf{h} + \delta_i + \delta_t$ ,	$\forall \mathbf{X} \in \Omega$ ,
$\mathbf{h} \cdot \mathbf{n}_0 = h_c(T - T_\infty)$ ,	$\forall \mathbf{X} \in \partial\Omega_c$ ,
$T = T_g$ ,	$\forall \mathbf{X} \in \partial\Omega_T$ ,
KKT system for plasticity: $\phi^p \leq 0$ ,	$\forall \mathbf{X} \in \Omega$ ,
$\dot{\bar{\epsilon}}^p \geq 0$ ,	$\forall \mathbf{X} \in \Omega$ ,
$\phi^p \dot{\bar{\epsilon}}^p = 0$ ,	$\forall \mathbf{X} \in \Omega$ ,
plastic flow rule: $\dot{\mathbf{F}}^p \mathbf{F}^{p-1} = \dot{\bar{\epsilon}}^p \mathbf{N}^p$ ,	$\forall \mathbf{X} \in \Omega$ ,
KKT system for fracture: $f_{,\nabla d}(d, \nabla d) \cdot \mathbf{n}_0 = 0$ ,	$\forall \mathbf{X} \in \partial\Omega$ ,
$\phi^f \leq 0$ ,	$\forall \mathbf{X} \in \Omega$ ,
$\dot{d} \geq 0$ ,	$\forall \mathbf{X} \in \Omega$ ,
$\phi^f d = 0$ ,	$\forall \mathbf{X} \in \Omega$ ,
initial conditions: $\phi(t=0) = \phi_0$ ,	$\forall \mathbf{X} \in \Omega$ ,
$\dot{\phi}(t=0) = 0$ ,	$\forall \mathbf{X} \in \Omega$ ,
$\mathbf{F}^p(t=0) = \mathbf{I}$ ,	$\forall \mathbf{X} \in \Omega$ ,
$T(t=0) = T_i$ ,	$\forall \mathbf{X} \in \Omega$ ,
$\bar{\epsilon}^p(t=0) = 0$ ,	$\forall \mathbf{X} \in \Omega$ ,
$d(t=0) = 0$ ,	$\forall \mathbf{X} \in \Omega$ .

The stress-strain relations, the KKT system for plasticity and the plastic flow rule are satisfied during constitutive updates within a standard finite element implementation. Therefore, the field equations (together with their initial and boundary conditions) to be discretized are:

### The strong form

governing equations: $\nabla \cdot \mathbf{P} + \rho_0 \mathbf{b} = \rho_0 \mathbf{a}$ ,	$\forall X \in \Omega$ ,
$\rho_0 c_v \dot{T} = -\nabla \cdot \mathbf{h} + \delta_i + \delta_t$ ,	$\forall X \in \Omega$ ,
$-\phi^f = \eta d - \nabla \cdot \left( \frac{2G_c l}{c_0} \nabla d \right) + \frac{\widehat{G}_c}{c_0 l} \alpha_{,d} + \Xi \geq 0$ ,	$\forall X \in \Omega$ ,
boundary conditions: $\mathbf{P} \mathbf{n}_0 = \mathbf{t}$ ,	$\forall X \in \partial\Omega_t$ ,
$\mathbf{h} \cdot \mathbf{n}_0 = h_c(T - T_\infty)$ ,	$\forall X \in \partial\Omega_c$ ,
$T = T_g$ ,	$\forall X \in \partial\Omega_T$ ,
$\mathbf{u} = \mathbf{u}_g$ ,	$\forall X \in \partial\Omega_u$ ,
$f_{,\nabla d} \cdot \mathbf{n}_0 = 0$ ,	$\forall X \in \partial\Omega$ ,
initial conditions: $\phi(t=0) = \phi_0$ ,	$\forall X \in \Omega$ ,
$\dot{\phi}(t=0) = 0$ ,	$\forall X \in \Omega$ ,
$T(t=0) = T_i$ ,	$\forall X \in \Omega$ ,
$d(t=0) = 0$ ,	$\forall X \in \Omega$ ,
constraints: $d \geq 0$ ,	$\forall X \in \Omega$ ,
$\phi^f \dot{d} = 0$ ,	$\forall X \in \Omega$ .

The weak form is developed with the aid of the following trial spaces  $\mathcal{U}_t$ ,  $\mathcal{T}_t$ , and  $\mathcal{D}_t$ :

$$\mathcal{U}_t = \{\mathbf{u} \in \mathcal{H}^1(\Omega)^d \mid \mathbf{u}(t) = \mathbf{u}_g \text{ on } \partial\Omega_u\}, \quad (37a)$$

$$\mathcal{T}_t = \{T \in \mathcal{H}^1(\Omega) \mid T = T_g \text{ on } \partial\Omega_T\}, \quad (37b)$$

$$\mathcal{D}_t = \{d \in \mathcal{H}^1(\Omega) \mid d \geq 0\}, \quad (37c)$$

and the accompanying weighting spaces  $\mathcal{V}$ ,  $\mathcal{E}$ , and  $\mathcal{Q}$ :

$$\mathcal{V} = \{\mathbf{w} \in \mathcal{H}^1(\Omega)^d \mid \mathbf{w}(t) = (\mathbf{0}) \text{ on } \partial\Omega_u\}, \quad (38a)$$

$$\mathcal{E} = \{e \in \mathcal{H}^1(\Omega) \mid e = 0 \text{ on } \partial\Omega_T\}, \quad (38b)$$

$$\mathcal{Q} = \{q \in \mathcal{H}^1(\Omega)\}. \quad (38c)$$

With a view towards the solution strategy, using a variational inequality solver (see 2.4), the below weak form for the damage subproblem only applies to the portion of the domain wherein  $\phi^f = 0$ . The weak form is given by:

### The weak form

Given  $\mathbf{u}_g$ ,  $t$ ,  $\bar{h}_c$ ,  $T_i$  and  $d_0$ , find  $\mathbf{u}(t) \in \mathcal{U}_t$ ,  $T \in \mathcal{T}_t$ , and  $d(t) \in \mathcal{D}_t$ ,  $t \in [0, t']$ , such that  $\forall \mathbf{w} \in \mathcal{V}$ ,  $\forall e \in \mathcal{E}$ , and  $\forall q \in \mathcal{Q}$ ,

$$\langle \mathbf{w}, t \rangle_{\partial\Omega_t} - (\nabla \mathbf{w}, \mathbf{P}) + (\mathbf{w}, \rho_0 \mathbf{b}) - (\mathbf{w}, \rho_0 \mathbf{a}) = 0, \quad (39a)$$

$$- (e, \rho_0 c_v \dot{T}) + (\nabla e, \mathbf{h}) + (e, \delta_i + \delta_t) = 0, \quad (39b)$$

$$(q, \eta d) + \left( \nabla q, \frac{2G_c l}{c_0} \nabla d \right) + \left( q, \frac{\widehat{G}_c}{c_0 l} \alpha_{,d} \right) + (q, \Xi) = 0, \quad (39c)$$

$$(\mathbf{w}, \phi(0) - \phi_0) = 0, \quad (39d)$$

$$(\mathbf{w}, \dot{\phi}(0)) = 0, \quad (39e)$$

$$(e, T(0)) - (e, T_i) = 0, \quad (39f)$$

$$(q, d(0)) = 0. \quad (39g)$$

Defining the following finite dimensional function spaces,  $\widetilde{\mathcal{U}}_t \subset \mathcal{U}_t$ ,  $\widetilde{\mathcal{T}}_t \subset \mathcal{T}_t$ ,  $\widetilde{\mathcal{D}}_t \subset \mathcal{D}_t$ ,  $\widetilde{\mathcal{E}}_t \subset \mathcal{E}_t$ ,  $\widetilde{\mathcal{Q}}_t \subset \mathcal{Q}_t$ , we use the Galerkin method to recover the spatially discretized form of the problem:

### The Galerkin form

Given  $\mathbf{u}_g$ ,  $t$ ,  $\bar{h}_c$ ,  $T_i$  and  $d_0$ , find  $\mathbf{u}^h(t) \in \widetilde{\mathcal{U}}_t$ ,  $T \in \widetilde{\mathcal{T}}_t$ , and  $d^h(t) \in \widetilde{\mathcal{D}}_t$ ,  $t \in [0, t']$ , such that  $\forall \mathbf{w}^h \in \widetilde{\mathcal{V}}$ ,  $\forall \mathbf{e}^h \in \widetilde{\mathcal{E}}$ , and  $\forall q^h \in \widetilde{\mathcal{Q}}$ ,

$$\langle \mathbf{w}^h, \mathbf{t} \rangle_{\partial\Omega_t} - (\nabla \mathbf{w}^h, \mathbf{P}) + (\mathbf{w}^h, \rho_0 \mathbf{b}) - (\mathbf{w}^h, \rho_0 \mathbf{a}) = \mathbf{0}, \quad (40a)$$

$$- (\mathbf{e}^h, \rho_0 c_v \dot{T}) + (\nabla \mathbf{e}^h, \mathbf{h}) + (\mathbf{e}^h, \delta_i + \delta_t) = \mathbf{0}, \quad (40b)$$

$$(q^h, \eta d) + \left( \nabla q^h, \frac{2G_c l}{c_0} \nabla d^h \right) + \left( q^h, \frac{\widehat{\mathcal{G}}_c}{c_0 l} \alpha_{d,d} \right) + (q^h, \Xi) = 0, \quad (40c)$$

$$(\mathbf{w}^h, \phi^h(0) - \phi_0) = 0, \quad (40d)$$

$$(\mathbf{w}^h, \dot{\phi}^h(0)) = 0, \quad (40e)$$

$$(\mathbf{e}^h, T^h(0)) - (\mathbf{e}^h, T_i) = 0, \quad (40f)$$

$$(q^h, d^h(0)) = 0. \quad (40g)$$

We note that this is a standard Galerkin approximation, in which identical functions are used to construct approximations to functions from both the trial and weighting spaces. The trial and weighting spaces are only different due to the boundary conditions, but in practice these too are approximated using functions from the same finite-dimensional set.

For temporal discretization, the Hilber–Hughes–Taylor- $\alpha$  (HHT- $\alpha$ ) method is employed for the balance of momentum [31]. HHT- $\alpha$  is selected for its ability to provide numerical damping and remove high-frequency noise from structural dynamics simulations without compromising second-order accuracy. Although the physical system has some damping due to plastic dissipation and heat conduction, this is confined to regions where the material has exceeded the yield point. Following the HHT- $\alpha$  method,  $\alpha_{\text{HHT}}$  is set to  $\frac{1}{3}$ , and as such  $\beta_{\text{HHT}} = \frac{(1-\alpha_{\text{HHT}})^2}{4}$  and  $\gamma_{\text{HHT}} = \frac{1}{2} - \alpha_{\text{HHT}}$  for all simulations. For the temporal discretization of the heat equation, a standard backward Euler method is employed.

### 2.4. Computational implementation

All simulations are performed using RACCOON [32], a massively parallel finite element code that specializes in phase-field fracture problems. RACCOON is built on the MOOSE framework [33], which was developed by Idaho National Laboratory. The mechanical and damage field problems are split into subproblems, which are solved using a fixed-point iteration solution scheme, as described by Hu et al. [30]. Both the thermo-mechanical and phase-field solvers use an absolute convergence criterion of  $1 \times 10^{-8}$  and a relative convergence criterion of  $1 \times 10^{-10}$ . The alternating scheme has an absolute tolerance of  $1 \times 10^{-6}$  and a relative tolerance of  $1 \times 10^{-8}$ .

The damage subproblem is solved using PETSc's variational inequality solver [34]. The irreversibility of the damage is enforced with a degree-of-freedom-wise primal-dual active-set strategy [35]. The KKT system for plasticity is implemented with a standard return mapping algorithm, while the F-bar method is used to alleviate volumetric locking, as described in de Souza Neto et al. [36].

## 3. Results

The sections below demonstrate the presented model's behavior in two-dimensional and three-dimensional simulations. All material properties are listed in Table 1 and are problem independent, with exceptions noted in each case. Bulk material properties and Johnson–Cook parameters are pulled from a work by Batra and Gummalla [37] as they characterize a high-strength steel at high strain-rates. Unless otherwise noted, the initial temperature  $T_i$  is taken to be equal to the reference temperature  $T_0$ . In these studies, the goal is to compare model behavior across different domains known for their shear behavior, rather than to replicate exact experimental results, however qualitative comparisons will be made. In this regard, the fracture properties listed in Table 1 are considered model parameters, and the sensitivity of the results to variations in them is examined herein.

### 3.1. Material response

To illustrate the interplay between plasticity, damage, and temperature in the model, an example problem in which all fields are spatially homogeneous is first examined. Consider a single eight-node brick (HEX8) element of size  $L \times L \times L$  subjected to uniaxial tension through a displacement boundary condition. The boundary value problem is constructed in such a way that the fields are spatially uniform in all directions, so that the gradients vanish and zero traction-boundary conditions are satisfied on the lateral surfaces. Such a boundary value problem essentially amounts to testing the bulk constitutive response of the material.

The material properties are listed in Table 1, and the characteristic dimension of the cube is taken to be  $L = 1$  mm. Based on (18), the critical fracture energy and the regularization length used in this section give rise to a nucleation energy of  $\psi_c = 37.5 \text{ mJ mm}^{-3}$ . For the sake of simplicity, heat generation is also neglected in this relatively simple example. For an assumed temperature of  $\frac{T}{T_m} = 0.27$  and an applied strain rate of  $\dot{\epsilon} = 1 \times 10^{-9} \mu\text{s}^{-1}$ , the model exhibits the  $\sigma_{zz}$  vs.  $\epsilon_{zz}$  response shown in Fig. 1. The stress is normalized by the quasi-static yield stress at the reference temperature,  $A$ , and the strain is normalized by the strain at which damage nucleates,  $\epsilon_d$ .

**Table 1**

Bulk material properties, fracture properties, and Johnson–Cook parameters. Bulk material properties and Johnson–Cook parameters are for a high-strength steel [37]. Fracture properties are viewed as model parameters.

Bulk material property	Symbol	Value	Unit
Bulk modulus	$K$	168 167	MPa
Shear modulus	$G$	77 615	MPa
Density	$\rho_0$	7900	$\mu\text{g mm}^{-3}$
Specific heat	$c_p$	$4.47 \times 10^{-4}$	$\text{mJ Mg}^{-1} \text{K}^{-1}$
Thermal conductivity	$\kappa$	$4.4 \times 10^{-4}$	$\text{kW mm}^{-1} \text{K}^{-1}$
Taylor–Quinney factor	$Q$	0.9	–
Fracture property			
Fracture toughness	$G_c$	20.0	$\text{mJ mm}^{-2}$
Residual degradation	$\eta$	$1 \times 10^{-6}$	–
Coalescence Param 1	$c_1$	0.5	–
Coalescence Param 2	$c_2$	0.1	–
Coalescence Param 3	$c_3$	0.1	–
Johnson–Cook parameter			
Reference yield stress	$A$	792.2	MPa
Strain hardening modulus	$B$	509.51	MPa
Strain rate sensitivity	$C$	0.014	–
Strain exponent	$n$	0.26	–
Temperature exponent	$m$	1.03	–
Reference temperature	$T_0$	280	K
Melting temperature	$T_m$	1033	K
Reference plastic strain rate	$\dot{\epsilon}_0^p$	$1 \times 10^{-6}$	$\mu\text{s}^{-1}$
Reference plastic strain	$\epsilon_0^p$	1	–

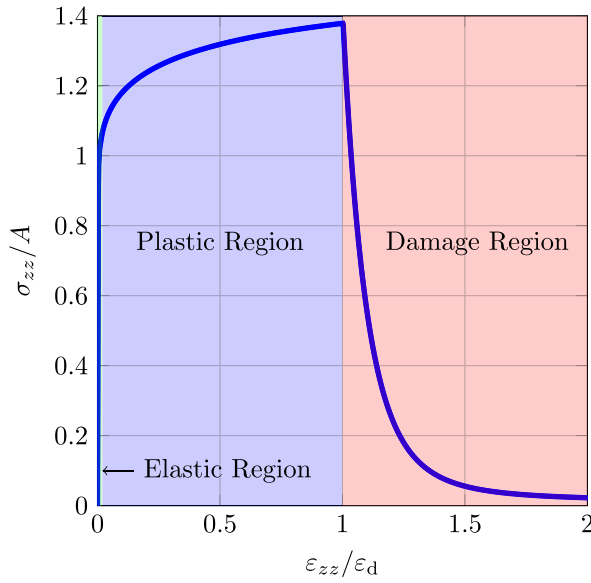


**Fig. 1.** Stress vs. strain response for uniaxial tension example.  $\varepsilon_d$  is the strain at damage nucleation.

The constitutive response can be separated into three distinct regimes: elastic, plastic, and plastic-damage. The elastic regime is present before yielding or damage occurs. The transition out of the elastic regime depends on the magnitude of the nucleation energy,  $\psi_c$ .

When the nucleation energy is sufficiently large so that it exceeds the elastic energy at the yield point,  $\psi_c > (A \cdot S(T))^2 / 2E$ , the constitutive response transitions from the elastic regime to the plastic regime, wherein the Johnson–Cook flow model governs the response. Damage nucleation subsequently occurs when  $w_{(A)}^e + w^p \geq \psi_c$ . Such a response, from elastic to plastic to damage is shown in Fig. 1. If instead the nucleation energy is sufficiently small so that  $\psi_c < (A \cdot S(T))^2 / 2E$ , then the model transitions from the elastic regime directly to the damage regime and no plastic flow occurs.

Using this same boundary-value problem, the sensitivity of the constitutive response to changes in the assumed temperature is now examined. Fig. 2 illustrates how the uniaxial stress–strain response varies as the temperature is increased relative to the melting temperature of the material, while keeping all other material and fracture properties the same. Again, the stress is normalized by

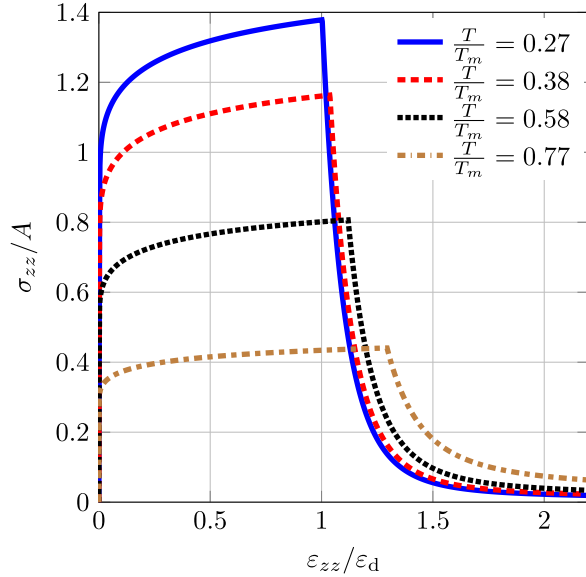


**Fig. 2.** Stress vs. strain response for homogeneous (uniaxial tension) example, at varying assumed temperatures.  $\epsilon_d$  is the strain at damage nucleation for  $\frac{T}{T_m} = 0.27$ .  $A$  is the quasi-static yield stress at  $\frac{T}{T_m} = 0.27$ .

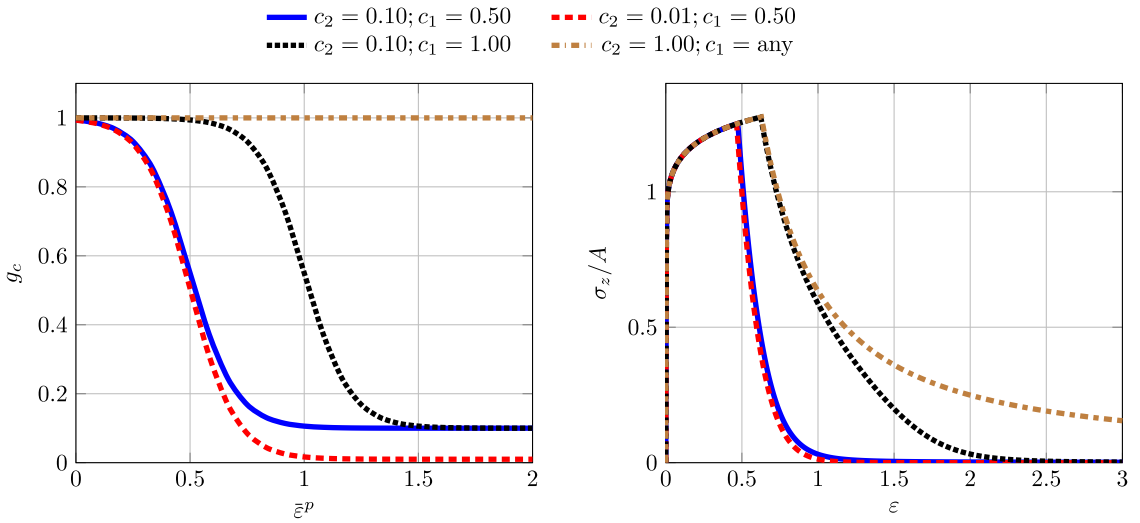


**Fig. 3.** Behavior of the coalescence function (left) and uniaxial stress-strain response (right) for various  $c_1$  and  $c_2$ . Default values are  $c_2 = 0.1$ ,  $c_1 = 0.5$ , and  $c_3 = 0.1$  (red curve). (For interpretation of the references to color in this figure legend, the reader is referred to the web version of this article.)

the quasi-static, reference temperature yield stress,  $A$ . The only modifier for the yield stress comes from the thermal degradation term,  $S(T)$ , as the strain rate is constant in these simulations. The results illustrate the inverse relationship between yield stress and temperature. Here, the Johnson–Cook model captures thermal softening through the thermal degradation term, parameterized by the melting and reference temperatures. As the assumed temperature increases, a noticeable decrease in yield stress is evident. Simultaneously, the strain at which damage initiates also increases. This trend is consistent with the typical behavior of metals, where higher temperatures lead to increased ductility, commonly known as thermal softening. This softening is quantitatively depicted in the figure by the progressive decrease in the normalized yield stress ( $\sigma_{zz}/A$ ) with increasing normalized temperature, ( $T/T_m$ ). Consequently, the reduced normalized yield stress reduces the active elastic energy, which delays fracture nucleation and leads to nucleation largely driven by plastic energy. Importantly, the shear band simulations examined in Sections 3.2 and 3.3 operate in the regime of  $\frac{T}{T_m} > 0.30$  once the temperature in the band increases due to thermo-mechanical coupling.

Fig. 3 illustrates how some of the parameters in the fracture model influence both the form of the coalescence function and the resulting stress–strain response. The coalescence function  $g_c$  is defined by three parameters:  $c_1$ ,  $c_2$ , and  $c_3$ . Specifically,  $c_1$  determines the plastic strain threshold at which this degradation begins;  $c_2$  governs the minimum value to which the critical fracture energy

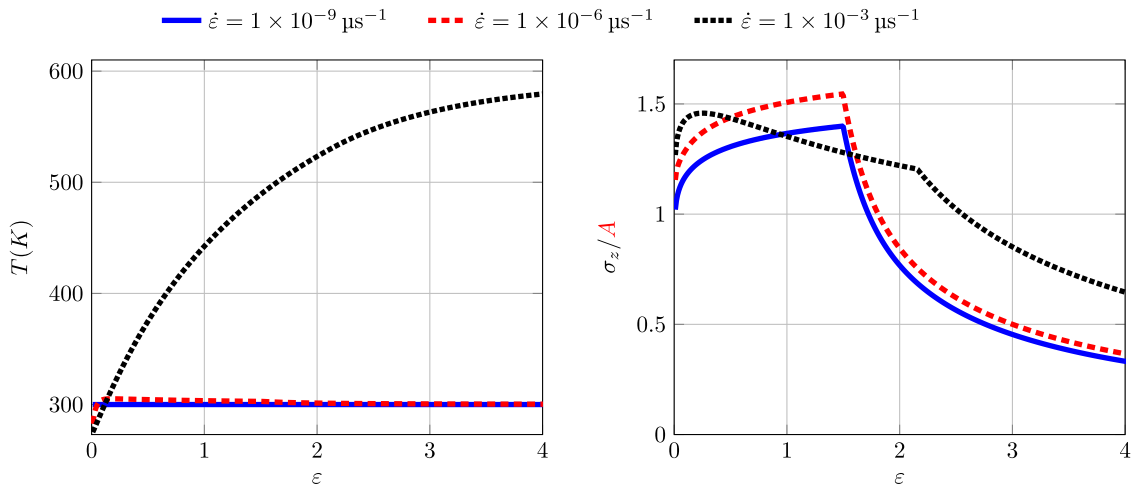


**Fig. 4.** Temperature (left) and stress response (right), for a single HEX8 element subjected to uniaxial stretch at varying strain rates, and with convective boundary conditions.

$G_c$  degrades and  $c_3$  sets the rate of this degradation process. The results shown in Fig. 3 are obtained by varying  $c_1$  and  $c_2$  while holding  $c_3$  constant. When  $c_2$  is set to 1, the coalescence function effectively becomes inactive, as indicated by  $g_c$  remaining at 1. This scenario corresponds to a gradual stress-strain decline during damage evolution, wherein rather large strains are needed for the damage to fully reach 1. Conversely, introducing the coalescence function with a relatively small  $c_2$ , as in the case with  $c_2$  set to 0.01, results in a markedly sharper decline in stress. This is a direct consequence of the coalescence function degrading  $G_c$  and effectively lowering the nucleation threshold for damage to begin. The influence of  $g_c$  on the nucleation energy is particularly noticeable when comparing cases with different  $c_1$  values, such as 0.5 and 1.0, combined with a  $c_2$  value of 0.1 (blue and red curves). For a sufficiently high  $c_1$  value, simulations with and without the coalescence function nucleate at the same strain (black and tan curves).

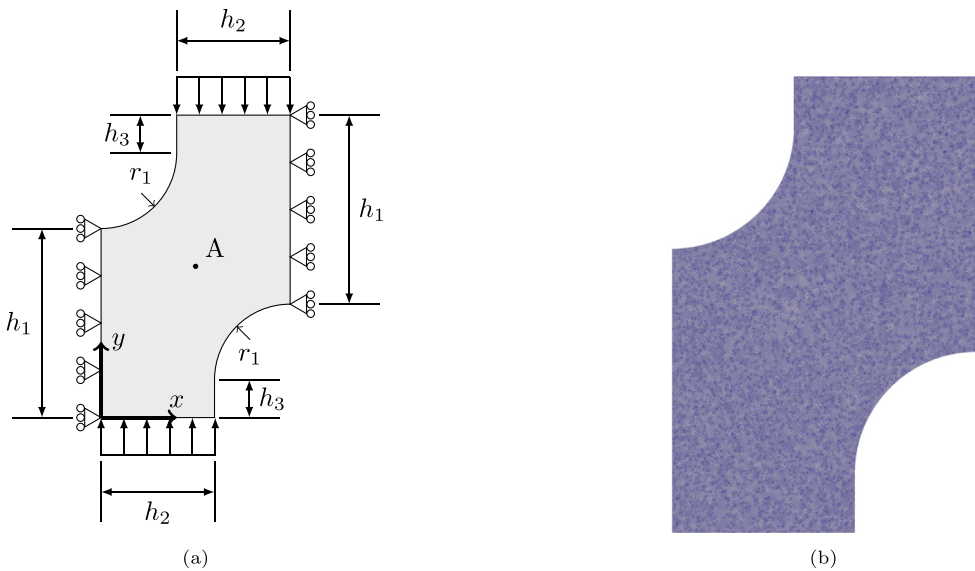
The rate-dependent properties of the model are now examined with the same boundary value problem, albeit with the displacement boundary condition adjusted to effect different strain rates. Heat generation from plastic dissipation is also included, and an external heat-convection boundary condition is applied to all surfaces with  $h_c = 1 \times 10^{-4} \text{ kW mm}^{-2} \text{ K}^{-1}$  and  $T_\infty = 300 \text{ K}$ .

Fig. 4 indicates the resulting temperature in the domain and the stress response for three different applied strain rates.  $\dot{\epsilon} = 1 \times 10^{-9} \mu\text{s}^{-1}$  represents a quasi-static case,  $\dot{\epsilon} = 1 \times 10^{-6} \mu\text{s}^{-1}$  represents an elevated strain rate, and  $\dot{\epsilon} = 1 \times 10^{-3} \mu\text{s}^{-1}$  represents strain rates seen in shear bands. The results serve to illustrate three distinct properties of the model: rate-dependent plasticity, rate-dependent heat generation, and the resulting impact on damage nucleation. The effects of the rate-dependent portion of the Johnson-Cook model are apparent in the yield stress of each case. As the strain rate is increased, the yield stress increases, up to about  $\approx 1.25A$ . The effects of rate-dependent heat generation are apparent when  $\dot{\epsilon} = 1 \times 10^{-6} \mu\text{s}^{-1}$  as heat generates faster than what is dissipated at the boundaries. As such, thermal softening affects the stress vs. strain response, seen through the drop in stress independent of any damage effects. Heat generation has a negligible effect on the lower strain rates as these strain rates cannot generate heat faster than that lost to the environment. Finally, damage nucleation is seen in each case as a sharp drop in strain rate. For  $\dot{\epsilon} = 1 \times 10^{-9} \mu\text{s}^{-1}$  and  $\dot{\epsilon} = 1 \times 10^{-6} \mu\text{s}^{-1}$  nucleation occurs at  $\epsilon \approx 1.5$ , while for  $\dot{\epsilon} = 1 \times 10^{-3} \mu\text{s}^{-1}$  nucleation occurs at  $\epsilon \approx 2.1$ . Recall that damage nucleation is driven by a combination of plastic energy and elastic energy in the model,  $w_{(A)}^e + w^p$ . The softening in the stress curve leads to a reduced active elastic energy in the high strain-rate case, thus delaying damage nucleation.

The dichotomy between the fast and slow responses is representative of the varying responses at material points inside and outside of a shear band, as has been well documented elsewhere [19,37–39]. The response to the high loading rate is the material response inside the shear band, and the response to the slow loading rate represents what is occurring adjacent to the shear band and in the rest of the domain. These results help illustrate the challenges associated with developing models in which damage nucleation and localization follow shear band formation.

### 3.2. Two-dimensional shear band problem

Consider the two-dimensional domain and loading shown in Fig. 5a, designed to create a region of intense shear between the two fillets. The dimensions are taken to be  $h_1 = 2.25 \text{ mm}$ ,  $h_2 = 1.5 \text{ mm}$ ,  $h_3 = 0.5 \text{ mm}$ , and  $r_1 = 1 \text{ mm}$ , and plane-strain conditions are assumed to hold. Displacement boundary conditions are applied to the top and bottom surfaces to induce a global strain rate of  $2 \times 10^{-3} \mu\text{s}^{-1}$ , which corresponds to a boundary velocity of  $3.75 \times 10^{-3} \text{ mm } \mu\text{s}^{-1}$ . This boundary-value problem is inspired by the classical “top hat” experiment as described in [40]. The simulated domain is reduced from the experimental domain to encompass only the region needed for shear band evolution. For the results that follow, the material properties are once again taken to be those provided in Table 1. These bulk material properties and Johnson-Cook parameters are representative of a high-strength steel [37],



**Fig. 5.** (a) Geometry and boundary conditions for the two-dimensional shear problem. Point A represents the geometric center of the domain. (b) Mesh for the case of  $h = 9.375 \times 10^{-4}$  mm. The refinement level corresponds to  $\frac{2\delta}{h} = 4.20$  in Fig. 6.

with the exception of the thermal conductivity  $\kappa$ , which is an order of magnitude larger than that of a typical steel (on the order of  $10^{-5}$  kW mm $^{-1}$  K [19,41,42]). Although the use of an artificially large thermal conductivity delays the temporal initiation of the shear band, it nevertheless facilitates spatial mesh convergence studies, as described below in Section 3.2.1.

The domain is discretized using an unstructured mesh of four-node quadrilateral elements, with the element count varying based on mesh resolution. A typical mesh is shown in Fig. 5b. Given the symmetry of the domain and the relative uniformity of the mesh, simulated shear bands are expected to pass through point A, which corresponds to the geometric center of the domain. Moreover, the point A is expected to be in the center of the band. This is in fact what the results below confirm, even though such an outcome was not artificially manufactured in any manner.

In what follows, results for the simulated width of the shear band are reported relative to an analytical estimate proposed by Dodd and Bai [38], given by

$$\delta \approx \left( \frac{\kappa \Delta T_*}{\sigma_{ij*} D_{ij*}} \right), \quad (41)$$

where  $\delta$  is the shear band half-width,  $\Delta T_*$  is the temperature rise within the shear band,  $D_{ij*}$  is the deformation rate tensor within the shear band, and  $\sigma_{ij*}$  is the stress within the shear band. This analytical estimate is the result of a two-dimensional perturbation analysis. It emphasizes the dependence of the shear band width on the combined stress state of the system, as well as the plastic dissipation and heat conduction. This estimate also implies that the width of the shear band is dynamic and can vary as the thermo-mechanical fields within the shear band evolve. Experimental observations for shear-band widths for steel range over 0.005 mm–0.05 mm [38,43]. In the following simulations, the calculated shear band width ranges from  $2\delta \approx 0.0078$  mm to  $2\delta \approx 0.0203$  mm, depending on the thermal conductivity parameter selected.

### 3.2.1. Mesh convergence study

This subsection provides results from a mesh convergence study into the shear band width, with an emphasis on the sensitivity to the degree of heat generation in the band and thermal diffusion out of it. For these results, coupling with damage is not considered, as the objective is to establish the resolution needed to achieve spatial convergence in the coupled thermo-mechanical fields alone. The following study iterates over a sequence of meshes of increasing refinement with characteristic mesh spacing  $h$ . The mesh sizes are normalized against the shear band half-width  $\delta$ , obtained from (41). The thermo-mechanical fields from the finest mesh are used to calculate  $\delta$ .

The temporal evolution of the effective plastic strain in the middle of the band (Point A in Fig. 5a) is shown in Fig. 6 for a sequence of refined meshes. In all cases, the results indicate that the effective plastic strain  $\varepsilon^p$  in the band exhibits a characteristic evolution with time. It rises steadily at early times, followed by a rapid increase, with accumulation over time decreasing once the shear band fully develops. The pattern is made clear by postprocessing the effective plastic strain to compute its second derivative with respect to time (using a central difference approximation), as shown in Fig. 6a. In particular, the second derivative of  $\varepsilon^p$  indicates a clear peak at various points in time, with the time to peak depending on the level of mesh resolution in the simulation. Peaks correspond to times of 30.84 μs, 28.94 μs, 27.49 μs, 27.19 μs, and 27.04 μs, indicative of a convergence to a time of approximately 27 μs. In what follows, this time to peak is used to make comparisons for the shear band width between meshes of differing resolutions. Such a

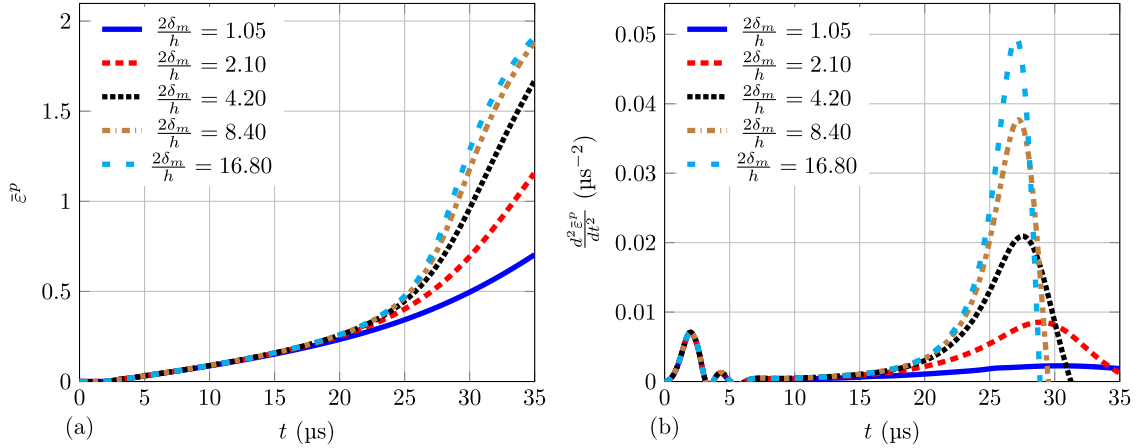


**Fig. 6.** Effective plastic strain (a) and second derivative of effective plastic strain (b) at the center of the shear band in the two-dimensional shear problem. Results are reported for various mesh spacings  $h$  relative to the width  $\delta_m$  of the shear band as determined by the simulation with the finest resolution.

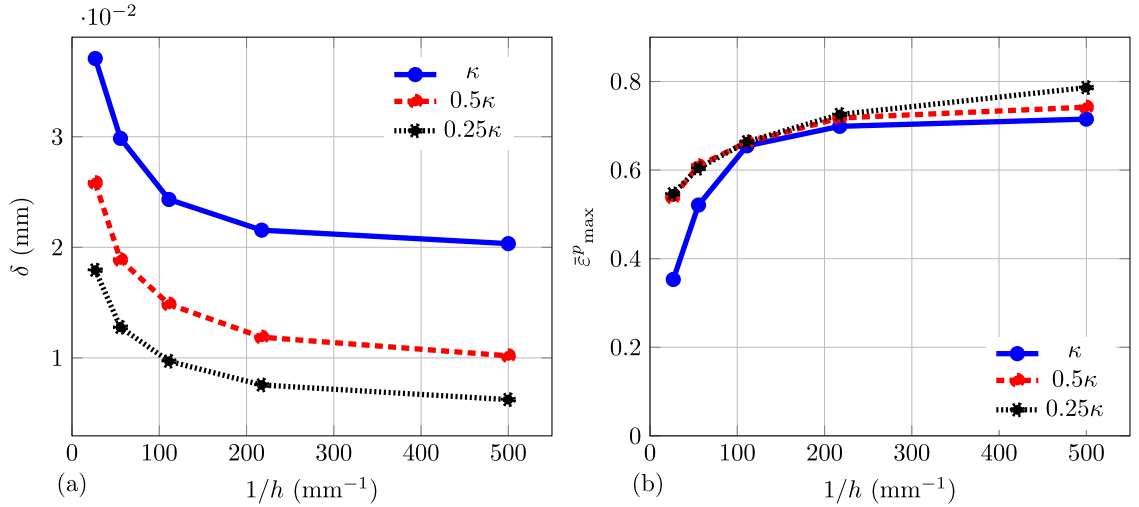


**Fig. 7.** Convergence of (a)  $\delta$  and (b)  $\bar{\varepsilon}^p_{\max}$  with mesh refinement, as a function of thermal conductivity  $\kappa$ , in the two-dimensional shear problem.

“second derivative criterion” is an extrapolation of the “two-phase” viewpoint discussed by Viswanathan et al. [11], in which a line of plastic strain first sets the orientation and direction of the shear band followed by the final collapse where the majority of plastic flow occurs.

Fig. 7 shows the variation in the simulated shear band width as a function of mesh resolution and thermal conductivity. Fig. 7a illustrates the trend of the half-width of the shear band with mesh refinement. As stated previously, data points are taken at the time of maximum  $\frac{d^2\bar{\varepsilon}^p}{dt^2}$  in the middle of the shear band at point A. Fig. 7a reveals that different thermal conductivity settings lead the shear band to converge to distinct widths, with the lowest conductivity displaying the lowest shear band width.

Fig. 7b illustrates how the maximum plastic strain value at the center of the shear band varies with mesh refinement and thermal conductivity. The results demonstrate that the peak  $\bar{\varepsilon}^p$  value diminishes as the thermal conductivity increases. In essence, larger thermal conductivities allow heat to diffuse out of the shear band, effectively limiting the temperature increase and the accompanying plastic flow. The peak values of the effective plastic strain converge with increasing mesh refinement. Mesh convergence is seen in the  $\kappa$  case, while the  $0.5\kappa$  and  $0.25\kappa$  have not fully converged with the refinements tested. Each curve is in a different stage of mesh convergence due to the differences in shear band width. For,  $0.25\kappa$ ,  $0.5\kappa$ ,  $\kappa$  at  $1/h = 500 \text{ mm}^{-1}$  the relative mesh ratios to the calculated shear band width are  $\frac{2\delta}{h} = 5.31$ ,  $\frac{2\delta}{h} = 8.69$ , and  $\frac{2\delta}{h} = 16.80$  respectively. The change from  $0.25\kappa$  to  $\kappa$  presents a 3.3x increase in refinement relative to their calculated shear band widths.

Fig. 8 displays various properties over the width of the shear band at the time where each simulation reaches a maximum  $\frac{d^2\bar{\varepsilon}^p}{dt^2}$  in the middle of the band. The displacement  $u_y$ , plastic strain  $\bar{\varepsilon}^p$ , and temperature  $T$  fields all localize in the vicinity of the shear band, where the elevated temperature and plastic flow together contribute to a collapse in the shear stress  $\sigma_{xy}$  at point A. More precisely, in the simulation with the most refined mesh, the shear stress in the band decreases by 5% below the maximum stress per  $\mu\text{s}$ . This

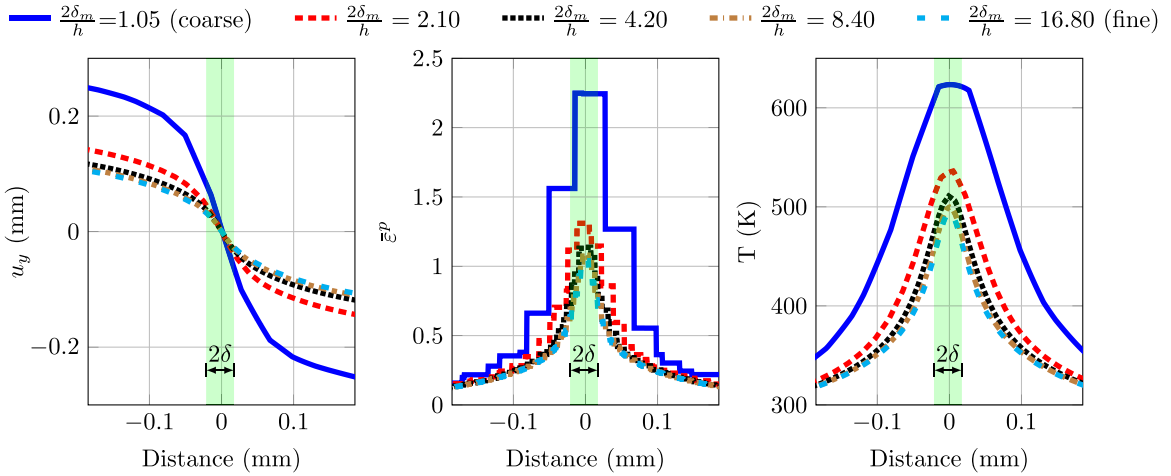


**Fig. 8.** Vertical displacement  $u_y$  (left), plastic strain (center), and temperature (right) taken over the width of the shear band for the two-dimensional shear problem. The green region represents the estimated shear band width (41).  $\delta_m$  is the shear band width from the most refined case. The granularity of the plastic strain plot corresponds to  $\bar{\epsilon}^p$  being a piecewise-constant state variable. (For interpretation of the references to color in this figure legend, the reader is referred to the web version of this article.)

shear stress collapse persists for approximately  $6\mu\text{s}$  before mesh distortion halts the simulation. The aforementioned behavior is qualitatively consistent with experimental observations [6,10,43,44]. The peak temperature  $T$  and effective plastic strain  $\bar{\epsilon}^p$  values both converge with increasing mesh refinement. Spatial convergence is seen to occur once  $1/h = 500\text{ mm}^{-1}$  which corresponds to  $\frac{2\delta}{h} \approx 17$ . It bears emphasis that this level of refinement is larger than what is typically employed to capture the length scale in phase-field models of fracture, in which  $\frac{2l}{h} = 5$  is often used.

From these observations, it can be concluded that the model can achieve spatial convergence after shear band collapse, provided the mesh resolution is sufficient to capture the thermo-mechanical coupling. The relationship between heat conduction and mesh convergence agrees with the theories proposed by Dodd and Bai [38] and Batra et al. [19], who postulate that heat conduction is required for shear band regularization.

### 3.2.2. Two-dimensional shear problem without damage coupling

For the sake of illustration, full-field results are now provided for the two-dimensional shear problem without any damage coupling. Figs. 9(a)–9(c) present the evolution of the shear band using a mesh with resolution  $\frac{2\delta}{h} = 18.5$  throughout the domain. The mesh consists of 403,576 elements with an average element size of  $h \approx 0.005\text{ mm}$ . The contours of the effective plastic strain are shown at times  $t = 15\mu\text{s}$ ,  $t = 22\mu\text{s}$ , and  $t = 27\mu\text{s}$ . Referring back to Fig. 6, these points in time correspond to moments before, during, and immediately after the shear stress collapse, represented by an increase in plastic flow, in the center of the shear band, labeled as Point P in Fig. 5. As described by Yadav and Sagapuram [10], the formation of the shear band showcases an initial homogeneous band that sets the orientation and direction, followed by a full collapse where the majority of the plastic flow occurs.

Figs. 10(a) and 10(b) display the temperature  $T$  and vertical displacement  $u_y$  fields just after the shear stress collapse, at  $t = 27\mu\text{s}$ . High temperatures can be seen to be localized to the regions of high plastic flow. Despite the effects of heat conduction, the width of the heated region is very narrow, corresponding closely with the width of the shear band. From the vertical displacement field, it is evident that the two halves of the sample are close to moving independently due to the shear band's elevated plastic flow (see Fig. 10).

It bears emphasis that the shear band evolves both temporally and spatially. As such, the behavior of material points in the shear band at the middle of the domain is different from that of material points in the band that are near the free surface. To illustrate this further, three points of interest are indicated in Fig. 9(c). The evolution of the effective plastic strain with time at each of these three points is shown in Fig. 11. The transition times of plastic flow at each location display distinct differences. Of note is the early transition time for the point at the free surface, location #1. This difference in transition time is important to note when considering the timing of damage nucleation, as discussed in the next Section.

### 3.2.3. Two-dimensional shear problem

Fully coupled results for the top hat problem are now presented, with an emphasis on the importance of the critical nucleation energy  $\psi_c$ . This critical energy represents a threshold that the combined elastic and plastic energies must exceed for damage to initiate. As such, smaller values of  $\psi_c$  will generally give rise to damage nucleation earlier in the process. As indicated by (18), the critical nucleation energy is governed by the ratio of the critical fracture energy  $G_c$  to the regularization length  $\ell$ . In the studies that follow, different nucleation energies are obtained by keeping the regularization length constant ( $l = 0.011\text{ mm}$ ) and adjusting  $G_c$  relative to the value listed in Table 1. Such a change influences crack propagation as well, but here the emphasis is on understanding how the threshold for damage nucleation significantly impacts the results.

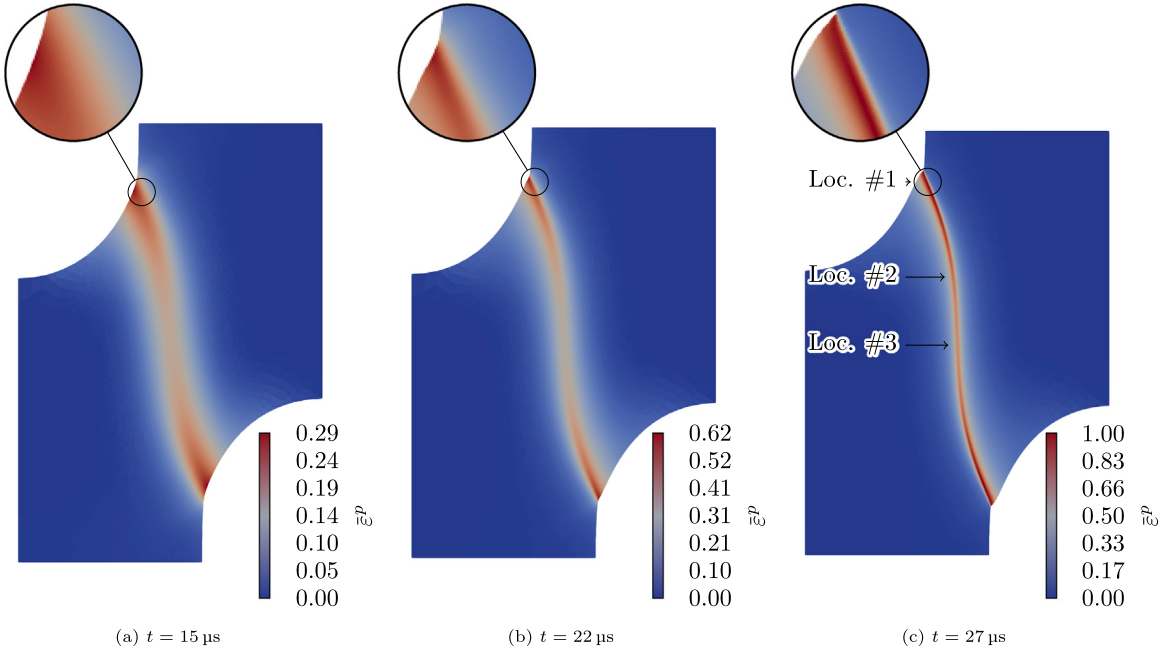


**Fig. 9.** Effective plastic strain fields in the two-dimensional shear problem (without damage coupling) at various points in time. Results shown were obtained using a mesh with uniform spacing  $\frac{2\delta}{h} = 18.5$ . Probed locations in Fig. 11 are indicated in (c). Locations #1, #2, and #3 have coordinates (1.000, 3.250), (1.171, 2.595) and (1.250, 1.875), respectively.

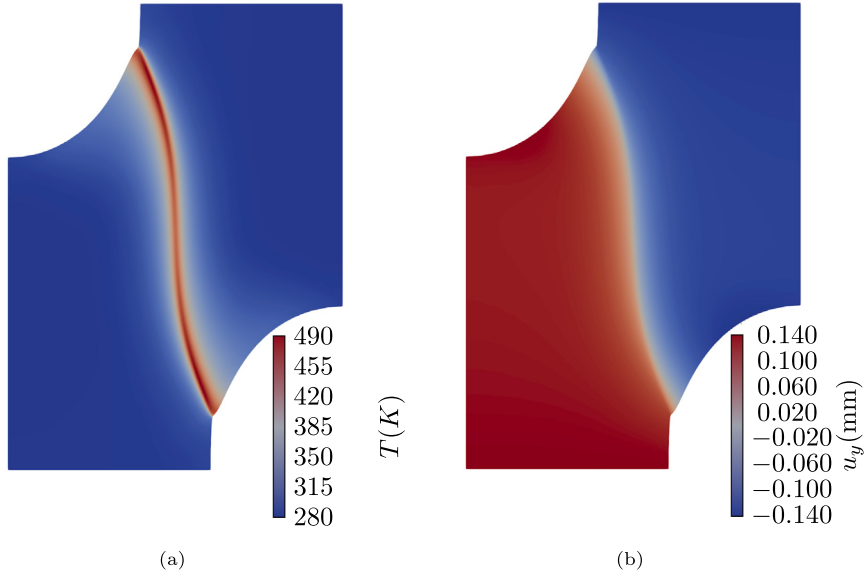


**Fig. 10.** Temperature  $T$  (a) and vertical displacement  $u_y$  (b) fields at  $t = 27 \mu s$  for a simulation of the two-dimensional shear problem with uniform mesh spacing  $\frac{2\delta}{h} = 16.8$ .

Fig. 12 displays the effective plastic strain and damage fields for the case where  $G_c = 0.2 \text{ mJ mm}^{-2}$  and  $\psi_c = 3.41 \text{ mJ mm}^{-3}$ . This relatively small value of  $\psi_c$  gives rise to a simulation in which damage nucleates before any appreciable plastic strain forms. Fig. 12(a) shows the contours of the effective plastic strain just before damage nucleation. At this early time, the plastic strain field is clearly much less localized than that shown in Fig. 9(c). At the location of first damage nucleation,  $w_{(A)}^e = 2.4 \text{ mJ mm}^{-3}$  and  $w^p = 1.1 \text{ mJ mm}^{-3}$ . The resulting response could be viewed as more of a brittle fracture than a ductile failure, in which the initiation and progression of damage occurs at a location and in an orientation distinct from the eventual shear band.

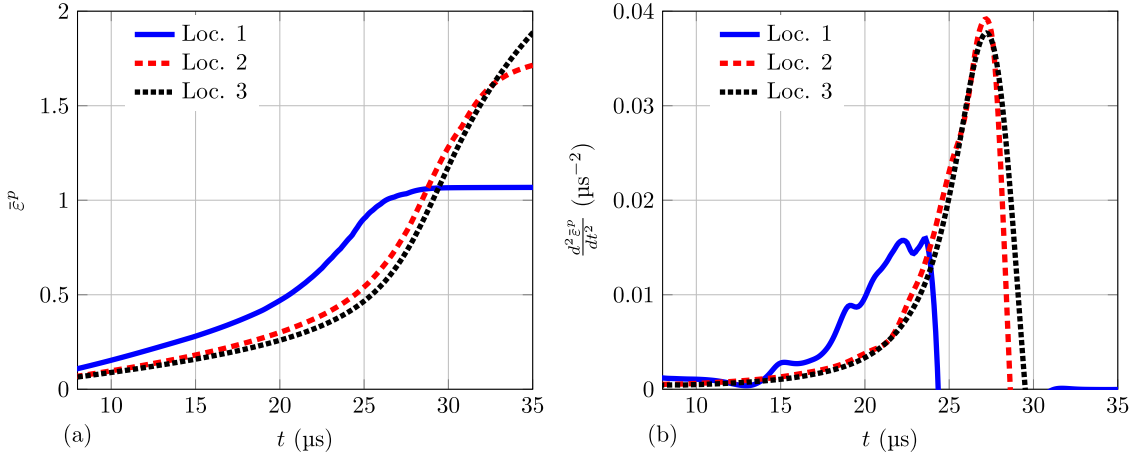


**Fig. 11.** Evolution of effective plastic strain (a) and the second derivative of plastic strain (b) vs. time at different locations along the shear band in the two-dimensional shear problem. Location 1 is at the free surface, and Location 3 is near the center of the domain, while Location 2 is in-between.

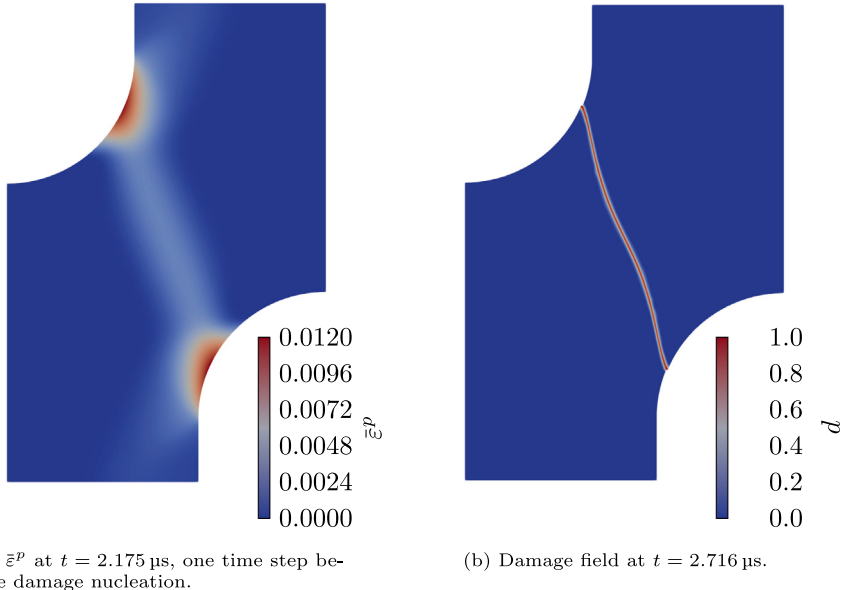


**Fig. 12.** Fully coupled results in the two-dimensional shear problem, obtained using a relatively small value of critical nucleation energy  $\psi_c = 3.41 \text{ mJ mm}^{-3}$ , giving rise to damage localization before stress collapse.

Fig. 13 displays the plastic strain and damage fields with  $G_c = 3.0 \text{ mJ mm}^{-2}$ , resulting in a considerably larger critical nucleation energy of  $\psi_c = 51.14 \text{ mJ mm}^{-3}$ . In this case, damage nucleation does not begin until the start of the shear band collapse. The effective plastic strain field just before damage nucleation is shown in Fig. 13(a). This field is clearly localized and close to that shown in Fig. 9(b) (shear band without damage). In this case, the location of damage nucleation shifts towards the edge of the curved surface, resulting in a crack trajectory that differs from that observed in Fig. 12(b). At the time and location of nucleation, the plastic energy exceeds the elastic energy,  $w_{(A)}^e = 3.1 \text{ mJ mm}^{-3}$  and  $w^p = 50 \text{ mJ mm}^{-3}$ . The high plastic strain leads to a fracture driven by plastic energy, with characteristics that are more typical for a ductile fracture. Note that the maximum damage shown in Fig. 13(b) is only  $d_{\max} \approx 0.7$ . This is as far as the simulation could proceed before mesh distortion at the edge of the domain became prohibitive. Additional refinement in the vicinity of the band was not observed to sufficiently ameliorate the issue in this case. Instead, what is likely required for simulations like these to continue concerns some form of adaptive remeshing, with state variable remapping, such as that described in [45].

The above results illustrate the sensitivity to different choices of the nucleation energy  $\psi_c$ . Importantly, they were both obtained using coalescence dissipation with the parameters  $c_1 = 0.5$  and  $c_2 = 0.1$  as indicated in Table 1. Analogous simulations without any coalescence dissipation (i.e.  $c_2 = 1$ ) tend to result in damage nucleation at much later times as well as a much slower damage localization. This follows from the removal of the plastic-damage coupling mechanism represented by (36c).

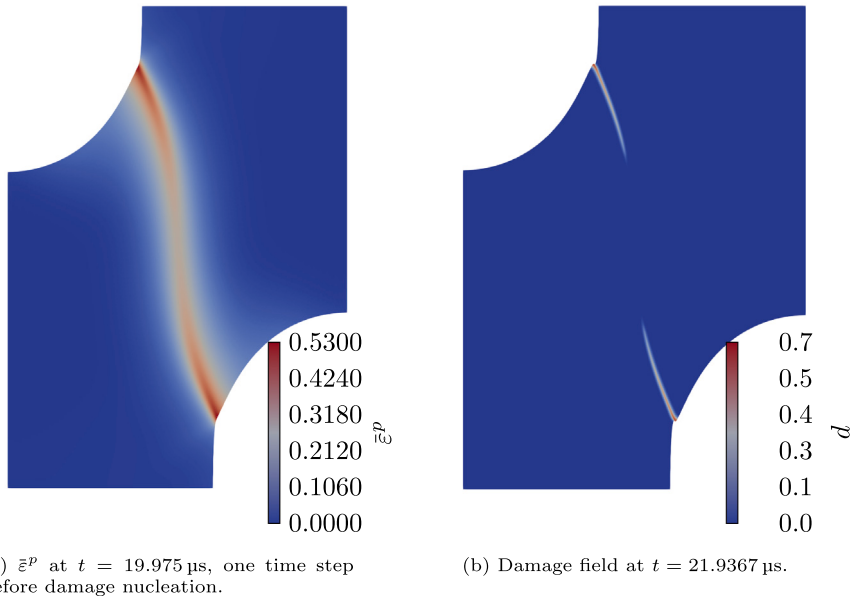


**Fig. 13.** Fully coupled results in the two-dimensional shear problem, obtained using a relatively large critical nucleation energy  $\psi_c = 51.14 \text{ mJ mm}^{-3}$ , giving rise to damage nucleation after shear band formation.

[Fig. 14](#) compares the paths of the damage field for early nucleation (red), late nucleation (blue), and the path of the shear band from [Fig. 9\(b\)](#) (dark gray). The location and orientation of the early damage band can be seen to differ significantly from that of the late damage band. The orientation of the late damage band is nearly parallel with the loading direction, indicating a pure shear failure. As indicated from the shadow of the effective plastic strain, this occurs due to the influence of the shear band on the late damage band.

[Fig. 15](#) displays the experimental results from Johansson et al. [40] for the original “top hat” problem. Some qualitative comparisons with the simulation results in [Fig. 14](#) can be made, even though the geometry and material properties are slightly different. The comparison is particularly good for the case of late nucleation (blue result in [Fig. 14](#)). For that case, it can be seen that in both the simulation and experiment, the shear band and crack nucleate at the edges of the top and bottom fillet. Additionally, as with the presented simulation results, Johansson et al. [40] note that “Before the occurrence of strain localization, the shear deformation is distributed over a larger volume...”, as well as an abrupt transition between homogeneous shear to the intense shear within the band itself. [Figs. 9\(a\)–9\(c\)](#) display a parallel to this behavior, as described previously.

### 3.3. Cylinder in torsion

Consider a hollow cylinder subjected to torsion as shown in [Fig. 16\(a\)](#). The dimensions are taken to be  $H = 2.50 \text{ mm}$ ,  $r_1 = 5.13 \text{ mm}$ , and  $r_2 = 4.75 \text{ mm}$ . The top surface is rotated about the  $z$ -axis, at an applied shear strain rate of  $\dot{\gamma} = 1600 \text{ s}^{-1}$  (equivalent to an angular velocity of  $\omega = 0.00078 \text{ rad } \mu\text{s}^{-1}$ ) while  $u_z = 0$  and the bottom surface is fixed in all directions. The bulk material and fracture properties are once again taken to be those given in [Table 1](#), with the exception of  $c_1$ ,  $C_c$ , and  $l$ , which are set to  $1$ ,  $10 \text{ mJ mm}^{-2}$ , and  $0.015 \text{ mm}$ , respectively. As described below, the effective plastic strain at the onset of the shear band is higher ( $\bar{\epsilon}^p \approx 0.9$ ) for this problem than that of the previous two-dimensional shear problem ( $\bar{\epsilon}^p \approx 0.4$ ). The shift in the coalescence function permits damage nucleation to occur after the formation of the shear band. This boundary value problem is inspired by the well-documented experiments conducted by Marchand and Duffy [6] and Duffy and Chi [46].

Without perturbation, this problem gives rise to spatially uniform fields. To force localization in the middle of the domain, a small spatial perturbation to the material properties is introduced. In this case, the reference yield stress  $A$  in the Johnson–Cook hardening law is perturbed according to

$$A = 750 - \frac{1}{2\pi\sigma_\theta\sigma_z\sqrt{1-\rho^2}} \exp \left[ -\frac{1}{4(1-\rho^2)} \left( \left( \frac{\theta-\mu_\theta}{\sigma_\theta} \right)^2 - 2\rho \left( \frac{\theta-\mu_\theta}{\sigma_\theta} \right) \left( \frac{z-\mu_z}{\sigma_z} \right) + \left( \frac{z-\mu_z}{\sigma_z} \right)^2 \right) \right],$$

corresponding to a bivariate Gaussian distribution in the  $z$  and  $\theta$  directions. Here,  $\theta = \arctan \frac{x}{y}$ ,  $\mu_\theta = 0$ ,  $\mu_z = 1.25$ ,  $\sigma_\theta = 0.08$ ,  $\sigma_z = 0.05$ , and  $\rho = 0$ . The perturbation is designed to force shear band formation parallel to the  $x$ – $y$  plane while also forcing initial localization at a point.

For this problem, a structured mesh of 145,112 HEX8 elements is created, as shown in [Fig. 16\(b\)](#). Mesh refinement is focused around the center of the domain where the shear band is expected to form, with additional local refinement applied near the point

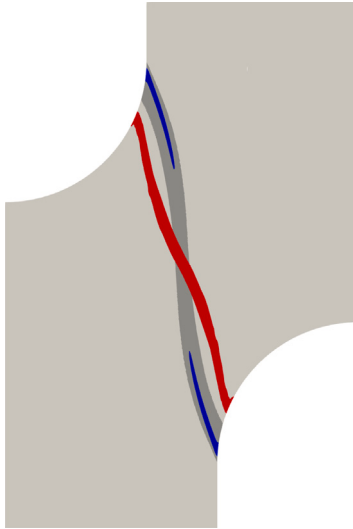


**Fig. 14.** Paths of damage for early nucleation (red) and nucleation after the shear band (blue) in fully coupled simulations of the two-dimensional shear problem. The path of the shear band is shown in dark gray. (For interpretation of the references to color in this figure legend, the reader is referred to the web version of this article.)

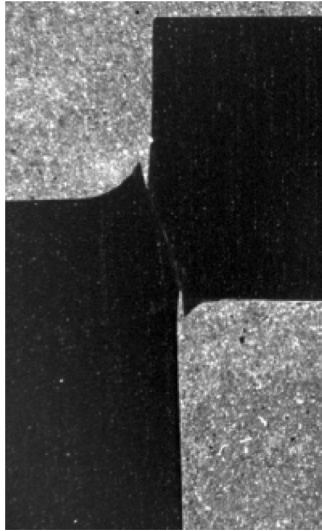


**Fig. 15.** Experimental results from Johansson et al. [40].

of damage nucleation. The mesh is pre-sheared in a direction opposite to the angle of twist in order to delay the onset of problematic mesh distortion.

A fully coupled response of the problem is simulated, using  $\psi_c = 125 \text{ mJ mm}^{-3}$ , which gives rise to a ductile type of failure. Figs. 17(a) and 17(b) illustrate the evolution of plastic strain from the onset of plastic flow transition to damage formation. Plastic strain is evident around the circumference, with heightened strains emerging in regions where the yield stress is perturbed. Localization begins at the outer surface of the cylinder and proceeds around the circumference. This is emphasized to show the directionality of the plastic strain formation before damage nucleation. A narrowing of the peak plasticity can be seen in Fig. 17(c), which corresponds to the time step just before damage nucleation. The localization of the region is characteristic of the transition from a homogeneous band of plastic strain to a localized shear band. This band continues to propagate around the circumference of the domain, followed by the propagation of damage (see Fig. 18).

Figs. 18(a)–18(c) illustrate the evolution of the damage band, with a focus on elements where  $d > 0.7$ , indicating a substantial reduction in stiffness. Damage forms where plastic strain is concentrated and follows the direction of the plastic strain. At  $t = 551 \mu\text{s}$ , the damage reaches  $d = 0.7$  and propagates outwards from the initial concentration of plastic strain. As time advances from  $t = 555 \mu\text{s}$  to  $t = 563 \mu\text{s}$ , the damage band becomes more pronounced and extends further, maintaining alignment with the trajectory of the

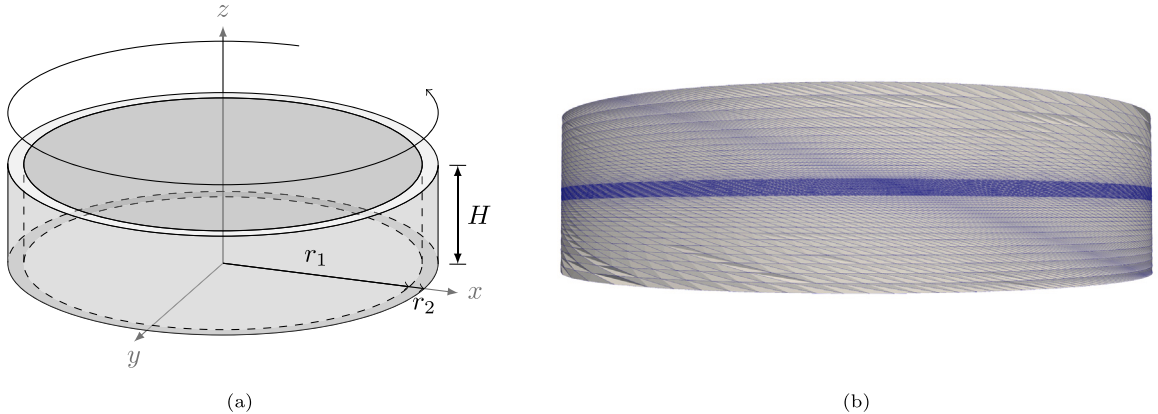


**Fig. 16.** Dimensions (a) and finite element mesh (b) of cylindrical specimen subjected to torsion. The mesh is pre-sheared in the direction opposite to the applied torsion.

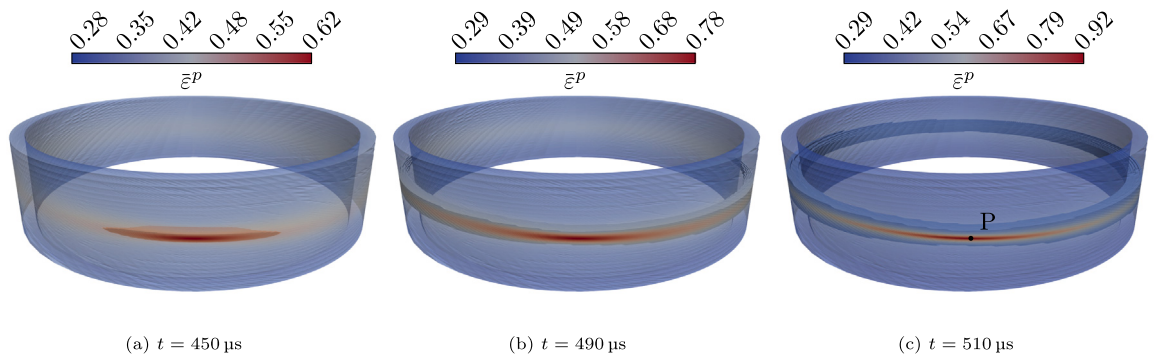


**Fig. 17.** Effective plastic strain fields at various points in time for the cylindrical torsion problem. Elements with  $\bar{\varepsilon}^p < 0.5$  are shown with reduced opacity.

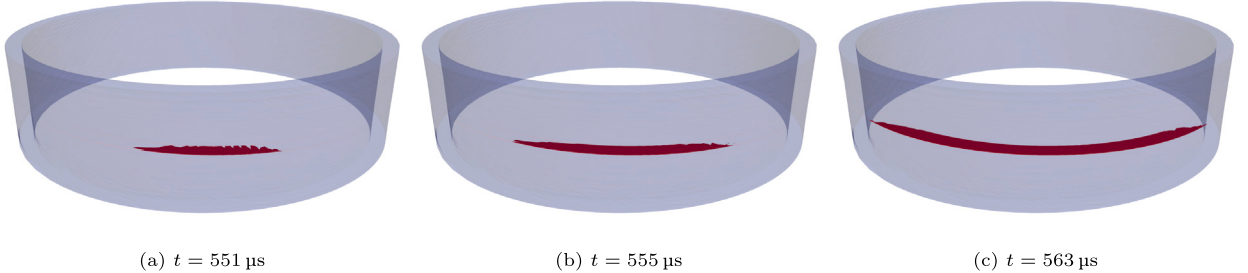


**Fig. 18.** Damage fields in the cylindrical torsion problem, for a fully coupled simulation. Damage fields are indicated where  $d > 0.7$ .

underlying plastic strain field. This alignment shows the plastic strain has an influence on both damage nucleation and directionality. The result at  $t = 563 \mu\text{s}$  displays the damage band after it propagated approximately a third of the circumference of the domain.

It is useful to compare some of the results for this problem, with and without damage coupling. Fig. 19a depicts the second derivative of the plastic strain with respect to time, sampled at the locus of maximum plastic strain as identified in Fig. 17(c) for both a simulation with damage coupling and without. The results for the case with damage are truncated after  $t = 520 \mu\text{s}$  due to noise in the data that obfuscates the trend. The undamaged case parallels the two-dimensional behavior of the second derivative of plastic strain as documented in Fig. 6 for the top hat problem, exhibiting an increase of plastic flow as the plastic strain localizes, followed by a deceleration of plastic flow as the shear band front progresses beyond the sampled point. Moreover, the increase and subsequent decrease of the second derivative of plastic strain occur in  $\approx 30 \mu\text{s}$ , with the increase starting at  $t = 500 \mu\text{s}$  and the decrease starting at  $t = 530 \mu\text{s}$ . The overall time span is comparable to the behavior of the two-dimensional shear band as discussed in Section 3.2. In the case with damage coupling, nucleation coincides with the onset of the flow transition at  $t = 510 \mu\text{s}$ . This result can therefore be considered to represent the formation of a shear band followed by damage localization, mimicking the observations recorded by Marchand and Duffy [6] and Duffy and Chi [46]. It is also worth noting that there is a coupling between the nucleation

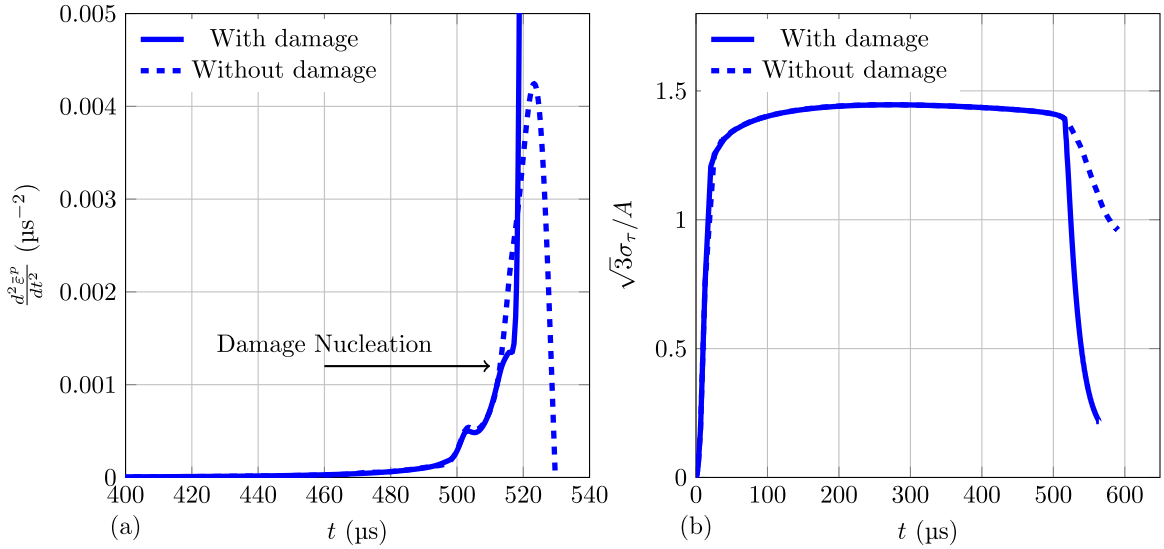


**Fig. 19.** Comparisons of various quantities for the cylindrical torsion problem, with and without damage coupling: (a) the second derivative of plastic strain at point P (shown in Fig. 17(c)) (b) the far-field shear stress vs. shear strain response, where  $\sigma_r = \sqrt{\sigma_{xz}^2 + \sigma_{yz}^2}$ . The vertical axis is normalized by the quasi-static reference temperature yield stress,  $A$ .

of damage and the plastic flow, in the sense that the damage further softens the material, giving rise to an even greater acceleration of the plastic strain (compared to the case without damage).

Fig. 19b displays the shear stress vs. time curves for simulations with and without damage. The shear stress is taken at a point on the top surface of the cylinder, where displacements are prescribed. As such, it represents the far-field conditions. Up until the time at the start of the shear band,  $t = 510 \mu\text{s}$ , both simulations display identical responses. Once damage nucleates, however, the combination of damage softening and thermal softening quickly drives the shear stress towards zero. By contrast, the simulation without damage coupling shows a much more gradual drop in stress after the onset of the shear band.

Previously, Batra and Zhang [47] conducted simulations using this same cylindrical geometry and observed that the shear band front accelerated non-linearly as it progressed around the specimen's circumference. Taking measurements at  $\theta = 0^\circ$  and  $\theta = 150^\circ$ , they observed speeds ranging from  $40 \text{ m/s}$  to  $260 \text{ m/s}$  at a loading speed of  $1000 \text{ s}^{-1}$ , to ranges of  $180 \text{ m/s}$  to  $1020 \text{ m/s}$  at a loading speed of  $5000 \text{ s}^{-1}$ . To better compare observations, the simulation without damage coupling is used for the following calculations. The shear band front is identified by taking  $\bar{\varepsilon}^p > 0.85$  to be the "front" of the shear band, as this is the plastic strain at  $\theta = 0^\circ$  at  $t = 510 \mu\text{s}$ . The shear band velocity is calculated as the time taken for the front to move  $\approx 10^\circ$  about the  $z$ -axis on the outer surface of the sample. Calculations performed at  $0^\circ$ ,  $90^\circ$ , and  $150^\circ$ , resulted in shear band velocities of approximately  $96 \text{ m/s}$ ,  $260 \text{ m/s}$ , and  $860 \text{ m/s}$ , respectively. The observed speeds display a non-linear acceleration of the shear band front through the sample, consistent with the results reported by Batra and Zhang [47].

We now provide a quantitative comparison of the simulated shear-stress behavior in this setup to the experimental results reported in Duffy and Chi [46], where the same torsional experiment was performed on a 4340 steel with various hardnesses. Fig. 20a provides a direct comparison of the stress-strain responses. Given the properties used for the model (Table 1), it is not surprising that there is a better comparison between the results in the early stages for the  $H_{RC} = 44$  case. Regardless, there is a significant difference in the strain at the time of shear stress collapse in both cases. This is likely due to many factors, such as differences in the material properties (e.g. the thermal conductivity) and the applied strain rates. But the primary difference is no doubt a result of the limited accuracy of the adopted Johnson-Cook model for the particular materials in these high-strain rate experiments.

Regardless, of primary interest to the current work concerns the response during shear stress collapse. Through a particular choice of normalization, several interesting features emerge. Fig. 20b compares the results by normalizing both the shear stresses and the shear strains. Namely, the experimental and simulation strains are normalized by the strain at the start of the shear band,  $\varepsilon_{\tau_{sb}}$ , and the stresses are normalized by appropriate yield stresses  $\sigma_{\tau0}$ . The experimental analysis used to determine the onset of shear band collapse results in more conservative time estimates than the shear stress collapse time calculated using Fig. 19,  $t = 510 \mu\text{s}$ . To compensate for this discrepancy, a shifted shear collapse time of  $t = 412 \mu\text{s}$  is used to normalize the simulation results, which corresponds to a shear strain of  $\varepsilon_{\tau_{sb}} = 0.66$ .

The normalized results in Fig. 20b highlight the ability of the model to capture the initial gradual softening of the shear stress curve before the final shear band collapse. The gradual softening is prominently present in the simulation without damage, where the only softening mechanism present is thermal softening. The simulation including damage has a much more drastic decrease in the stress as damage introduces an additional softening mechanism. The difference in behavior is analogous to that noted by Duffy

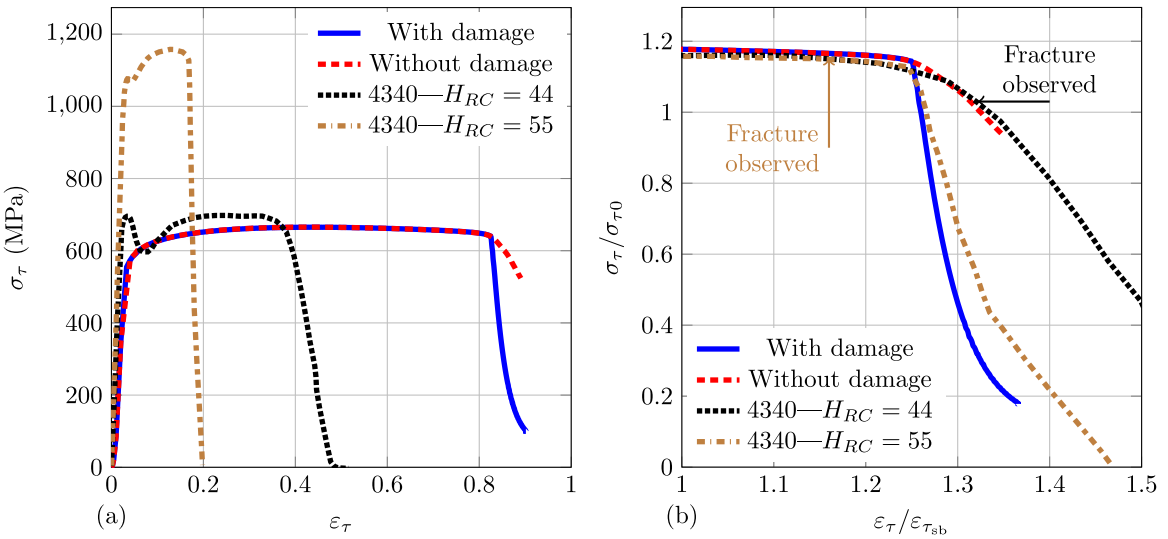


**Fig. 20.** Comparison of global shear stress behavior at the shear band collapse for the finite-element simulation and an experiment on two kinds of 4340 steel, as reported by Duffy and Chi [46], with hardnesses,  $H_{RC} = 44, 55$ . (a) The shear stress vs. shear strain response for the simulation and both experiments. (b) Normalized plots of each case's shear band collapse. The vertical axis is the far-field shear stress  $\sigma_\tau = \sqrt{\sigma_{xz}^2 + \sigma_{yz}^2}$  normalized by their apparent yield stress in shear,  $\sigma_{\tau_0}$ . The yield stress  $\sigma_{\tau_0} = 560$  MPa for the simulation. For the experiments, the values of the yield stress used are; 600 MPa for  $H_{RC} = 44$  and 1000 MPa for  $H_{RC} = 55$ . The horizontal axis is the shear strain  $\varepsilon_\tau$  normalized by the shear strain value at the start of shear band collapse  $\varepsilon_{\tau_{sb}}$ . The shear strain  $\varepsilon_{\tau_{sb}} = 0.66$  for the simulation and, as reported by Duffy and Chi,  $\varepsilon_{\tau_{sb}} = 0.30$  for  $H_{RC} = 44$  and  $\varepsilon_{\tau_{sb}} = 0.14$  for  $H_{RC} = 55$ . The two arrows indicate where fracture was first reported in the experiments.

and Chi for the two different steels. For the steel with hardness  $H_{RC} = 44$ , from the first observed shear band, 60  $\mu$ s passes before a crack is observed, at which point the shear band collapse has already begun. However, in the more brittle steel with hardness  $H_{RC} = 55$ , fracture is confirmed within 20  $\mu$ s of the first observed shear band. Importantly, fracture is noted before the stress collapse is observed. One can conclude that the sharp drop in the  $H_{RC} = 55$  case is due to the presence of significant fracture within the shear band, while the slower drop in the  $H_{RC} = 44$  case results from the absence of such fracture at the start of the shear band collapse. These observations highlight the importance of differentiating both cases and how they can be effectively bracketed by the model.

Fig. 21 displays a qualitative comparison between the simulation results and the experimental observations described in Marchand and Duffy [6]. For the simulation results, the white lines indicate contours of angular displacement on the outer surface of the domain. A comparison is made at various points in time to illustrate the various stages of deformation. The most straightforward point of comparison is during the homogeneous stage, shown in Figs. 21(a) and 21(b), where no significant localization has occurred. Both simulation and experiment display mostly straight displacement lines. The color contours in Fig. 21(a) indicate the effective plastic strain and illustrate the onset of yielding. This is not verifiable in the corresponding experimental image, although it obviously begins at some point.

Figs. 21(c) and 21(d) display a transition to inhomogeneous deformation, which represents the start of the shear band formation (see Fig. 19 at  $t = 510 \mu$ s). Due to the way the material is locally perturbed, the plastic and damage bands are not forced to be aligned along the center of the sample, and thus, a tilt in the angle of each is seen. The simulation displays a narrowing of the region of plastic strain, and it appears that the physical sample is experiencing a similar effect, given the distorted deformation fields evident in Fig. 21(d). Additionally, thermal softening is beginning to affect the global response, as indicated by Fig. 19b at the onset of the stress collapse. The final collapse is represented in Figs. 21(e) and 21(f). Experimental contours display a severe jump in displacement across the shear band. The simulated results do not display quite as severe a distortion as the experimental results due to the limitations imposed by mesh distortion.

As a final remark in this section, we note that comparable qualitative comparisons to this experiment could certainly be made with other models that are not developed within a phase-field for fracture or variational setting. These include, for example, models for ductile fracture that account for various mechanisms such as void volume fraction or porosity and interpret them as damage [48,49]. The extent to which the incorporation of such models into the current framework might yield both strong qualitative and quantitative comparisons with experimental observations is an area for future work.

#### 4. Conclusion

In this work, we extended the framework outlined by Hu et al. [3] through the inclusion of a temperature field, thermal softening, and dissipative effects. The combination of additional physics allowed for the mesh-insensitive simulation of shear band formation,

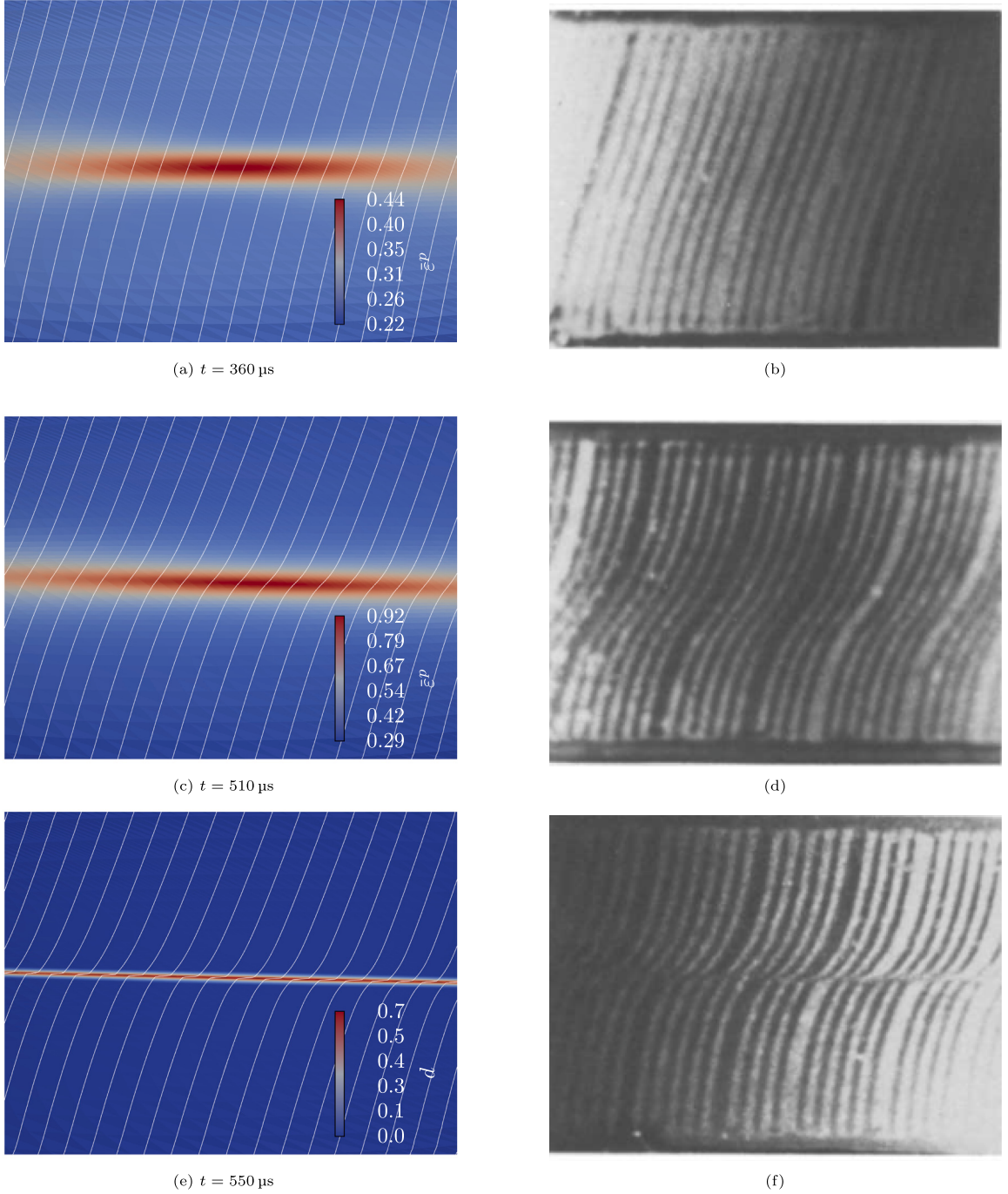


**Fig. 21.** Comparison of angular displacements for simulation results (a, c, and e) and experimental results for Marchand and Duffy [6] (b, d, and f) at various stages of collapse. For the simulation results, the white lines indicate contours of angular displacements on the outer surface of the specimen, while the color contours denote the effective plastic strain (a and c) or the damage (e). (For interpretation of the references to color in this figure legend, the reader is referred to the web version of this article.)

which is a failure mode characterized by high temperatures and high plastic flow. Dissipative terms naturally fall out of the rate-dependent form of the Johnson–Cook model when cast into a variational framework. The resulting dissipative terms lead to heat generation with plastic flow. Our results indicated that mesh convergence in various quantities of interest can be obtained with

this method, but that extremely refined meshes are often required. Further, the level of mesh resolution needed to attain spatial convergence in the shear band tends to scale with various material properties, such as the thermal conductivity.

A gradient damage model was utilized within a standard AT-1 formulation and a quadratic degradation function. These choices give rise to a model in which damage nucleation is governed by an energetic threshold. The model's efficacy in simulating rate-dependent material response was demonstrated through a series of simulations of various boundary-value problems, with and without damage coupling. This includes a study of the bulk constitutive response, a two-dimensional shear band problem demonstrating mesh convergence, and a three-dimensional problem. With a judicious choice of model parameters, these simulations demonstrated how the model can exhibit a transition from shear band formation to fracture, qualitatively consistent with several experimental observations in this area. Of course, quantitative comparisons with actual experiments require considerable parameter calibration, an exercise that can be a significant challenge for problems in this domain.

The results and model development in this work point toward several areas for future work. Mesh distortion was observed to prohibit computations from proceeding in several cases, and as demonstrated by Batra and Jin [50] and Batra and Ko [51], the use of remesh-and-remap strategies can circumvent this issue. Another possibility concerns a departure from an energetic damage threshold to one based on a strength surface, such as that proposed by Kumar et al. [52]. A strength surface would give more control on the conditions of damage nucleation as well as the potential to implement further influences on damage nucleation, such as stress-triaxiality. Recent work by Larsen et al. [53] has shown how a strength-based model can also be cast in a variational framework.

#### CRediT authorship contribution statement

**David E. Torres:** Writing – original draft, Software, Investigation. **Tianchen Hu:** Writing – review & editing, Project administration, Formal analysis, Conceptualization. **Andrew J. Stershic:** Writing – review & editing, Supervision, Methodology. **Timothy R. Shelton:** Writing – review & editing, Project administration. **John E. Dolbow:** Writing – review & editing, Writing – original draft, Supervision, Project administration, Methodology, Investigation, Funding acquisition, Formal analysis, Conceptualization.

#### Declaration of competing interest

The authors declare that they have no known competing financial interests or personal relationships that could have appeared to influence the work reported in this paper.

#### Acknowledgments

The authors would like to acknowledge several helpful comments and conversations with Professor Romesh Batra, of Virginia Tech, during the review stage of this manuscript.

The support of Sandia National Laboratories, to Duke University, is gratefully acknowledged. Sandia National Laboratories is a multi-mission laboratory managed and operated by National Technology & Engineering Solutions of Sandia, LLC (NTESS), a wholly owned subsidiary of Honeywell International Inc., for the U.S. Department of Energy's National Nuclear Security Administration (DOE/NNSA) under contract DE-NA0003525. This written work is authored by an employee of NTESS. The employee, not NTESS, owns the right, title and interest in and to the written work and is responsible for its contents. Any subjective views or opinions that might be expressed in the written work do not necessarily represent the views of the U.S. Government. The publisher acknowledges that the U.S. Government retains a non-exclusive, paid-up, irrevocable, world-wide license to publish or reproduce the published form of this written work or allow others to do so, for U.S. Government purposes. The DOE will provide public access to results of federally sponsored research in accordance with the DOE Public Access Plan.

#### Data availability

Data will be made available on request.

#### References

- [1] M. Arriaga, H. Waisman, Combined stability analysis of phase-field dynamic fracture and shear band localization, *Int. J. Plast.* 96 (2017) 81–119, <http://dx.doi.org/10.1016/j.ijplas.2017.04.018>.
- [2] C. Miehe, M. Hofacker, L.-M. Schänzel, F. Aldakheel, Phase field modeling of fracture in multi-physics problems. Part II. Coupled brittle-to-ductile failure criteria and crack propagation in thermo-elastic-plastic solids, *Comput. Methods Appl. Mech. Engrg.* 294 (2015) 486–522, <http://dx.doi.org/10.1016/j.cma.2014.11.017>.
- [3] T. Hu, B. Talamini, A.J. Stershic, M.R. Tupek, J.E. Dolbow, A variational phase-field model for ductile fracture with coalescence dissipation, *Comput. Mech.* 68 (2) (2021) 311–335, <http://dx.doi.org/10.1007/s00466-021-02033-1>.
- [4] G. Francfort, J.-J. Marigo, Revisiting brittle fracture as an energy minimization problem, *J. Mech. Phys. Solids* 46 (8) (1998) 1319–1342, [http://dx.doi.org/10.1016/S0022-5096\(98\)00034-9](http://dx.doi.org/10.1016/S0022-5096(98)00034-9).
- [5] B. Bourdin, G. Francfort, J.-J. Marigo, Numerical experiments in revisited brittle fracture, *J. Mech. Phys. Solids* 48 (4) (2000) 797–826, [http://dx.doi.org/10.1016/S0022-5096\(99\)00028-9](http://dx.doi.org/10.1016/S0022-5096(99)00028-9).
- [6] A. Marchand, J. Duffy, An experimental study of the formation process of adiabatic shear bands in a structural steel, *J. Mech. Phys. Solids* 36 (3) (1988) 251–283, [http://dx.doi.org/10.1016/0022-5096\(88\)90012-9](http://dx.doi.org/10.1016/0022-5096(88)90012-9).

- [7] D.C. Pagan, M. Obstalecki, J.-S. Park, M.P. Miller, Analyzing shear band formation with high resolution X-ray diffraction, *Acta Mater.* 147 (2018) 133–148, <http://dx.doi.org/10.1016/j.actamat.2017.12.046>.
- [8] J. Desrues, P. Bésuelle, H. Lewis, Strain localization in geomaterials, *Geol. Soc. Lond. Special Publ.* 289 (1) (2007) 47–73, <http://dx.doi.org/10.1144/SP289.4>.
- [9] C. Zener, J.H. Hollomon, Effect of strain rate upon plastic flow of steel, *J. Appl. Phys.* 15 (1) (1944) 22–32, <http://dx.doi.org/10.1063/1.1707363>.
- [10] S. Yadav, D. Sagapuram, *In Situ* analysis of shear bands and boundary layer formation in metals, *Proc. R. Soc. A* 476 (2234) (2020) 20190519, <http://dx.doi.org/10.1098/rspa.2019.0519>.
- [11] K. Viswanathan, S. Yadav, D. Sagapuram, Shear bands in materials processing: Understanding the mechanics of flow localization from zener's time to the present, *Appl. Mech. Rev.* 72 (6) (2020) 060802, <http://dx.doi.org/10.1115/1.4049353>.
- [12] H. Ratteez, I. Stefanou, J. Sulem, M. Veveakis, T. Poulet, The importance of thermo-hydro-mechanical couplings and microstructure to strain localization in 3D continua with application to seismic faults. Part II: Numerical implementation and post-bifurcation analysis, *J. Mech. Phys. Solids* 115 (2018) 1–29, <http://dx.doi.org/10.1016/j.jmps.2018.03.003>.
- [13] A.B. Jacquay, H. Ratteez, M. Veveakis, Strain localization regularization and patterns formation in rate-dependent plastic materials with multiphysics coupling, *J. Mech. Phys. Solids* 152 (2021) 104422, <http://dx.doi.org/10.1016/j.jmps.2021.104422>.
- [14] R. De Borst, L.J. Sluys, H.-B. Muhlhaus, J. Pamin, Fundamental issues in finite element analysis of localization of deformation, *Eng. Comput.* 10 (2) (1993) 99–121, <http://dx.doi.org/10.1108/ebo023897>.
- [15] O. Dillon, J. Kratochvil, A strain gradient theory of plasticity, *Int. J. Solids Struct.* 6 (12) (1970) 1513–1533, [http://dx.doi.org/10.1016/0020-7683\(70\)90061-2](http://dx.doi.org/10.1016/0020-7683(70)90061-2).
- [16] E.C. Aifantis, The physics of plastic deformation, *Int. J. Plast.* 3 (3) (1987) 211–247, [http://dx.doi.org/10.1016/0749-6419\(87\)90021-0](http://dx.doi.org/10.1016/0749-6419(87)90021-0).
- [17] S. Forest, J.-S. Blazy, Y. Chastel, F. Moussy, Continuum modeling of strain localization phenomena in metallic foams, *J. Mater. Sci.* 40 (22) (2005) 5903–5910, <http://dx.doi.org/10.1007/s10853-005-5041-6>.
- [18] W.M. Wang, L.J. Sluys, R. De Borst, Interaction between material length scale and imperfection size for localization phenomena in viscoplastic media, *Eur. J. Mech. A Solids* 15 (3) (1996) 447–464.
- [19] R. Batra, C. Kim, Effect of thermal conductivity on the initiation, growth and bandwidth of adiabatic shear bands, *Internat. J. Engrg. Sci.* 29 (8) (1991) 949–960, [http://dx.doi.org/10.1016/0020-7225\(91\)90168-3](http://dx.doi.org/10.1016/0020-7225(91)90168-3).
- [20] T.W. Wright, R.C. Batra, The initiation and growth of adiabatic shear bands, *Int. J. Plast.* 1 (1985) 205–212.
- [21] M.J. Borden, T.J. Hughes, C.M. Landis, A. Anvari, I.J. Lee, A phase-field formulation for fracture in ductile materials: Finite deformation balance law derivation, plastic degradation, and stress triaxiality effects, *Comput. Methods Appl. Mech. Engrg.* 312 (2016) 130–166, <http://dx.doi.org/10.1016/j.cma.2016.09.005>.
- [22] T. Wang, Z. Liu, Y. Cui, X. Ye, X. Liu, R. Tian, Z. Zhuang, A thermo-elastic-plastic phase-field model for simulating the evolution and transition of adiabatic shear band. Part I. Theory and model calibration, *Eng. Fract. Mech.* 232 (2020) 107028, <http://dx.doi.org/10.1016/j.engfracmech.2020.107028>.
- [23] G.R. Johnson, W.H. Cook, Fracture characteristics of three metals subjected to various strains, strain rates, temperatures and pressures, *Eng. Fract. Mech.* 21 (1) (1985) 31–48, [http://dx.doi.org/10.1016/0013-7944\(85\)90052-9](http://dx.doi.org/10.1016/0013-7944(85)90052-9).
- [24] L. Ambrosio, V.M. Tortorelli, Approximation of functional depending on jumps by elliptic functional via T-convergence, *Comm. Pure Appl. Math.* 43 (8) (1990) 999–1036, <http://dx.doi.org/10.1002/cpa.3160430805>.
- [25] C. McAuliffe, H. Waisman, Mesh insensitive formulation for initiation and growth of shear bands using mixed finite elements, *Comput. Mech.* 51 (5) (2013) 807–823, <http://dx.doi.org/10.1007/s00466-012-0765-z>.
- [26] Q. Yang, L. Stainer, M. Ortiz, A variational formulation of the coupled thermo-mechanical boundary-value problem for general dissipative solids, *J. Mech. Phys. Solids* 54 (2) (2006) 401–424, <http://dx.doi.org/10.1016/j.jmps.2005.08.010>.
- [27] G.R. Johnson, W.H. Cook, A constitutive model and data for metals subjected to large strain, high strain rates and high temperatures, in: Proceedings of the 7th International Symposium on Ballistics, American Defense Preparedness Association, The Hague, Netherlands, 1983.
- [28] T. Hu, A Variational Framework for Phase-Field Fracture Modeling with Applications to Fragmentation, Dessication, Ductile Failure, and Spallation, (PhD thesis), PhD dissertation, Duke University, 2021.
- [29] S. Matsubara, K. Terada, A variationally consistent formulation of the thermo-mechanically coupled problem with non-associative viscoplasticity for glassy amorphous polymers, *Int. J. Solids Struct.* 212 (2021) 152–168, <http://dx.doi.org/10.1016/j.ijsolstr.2020.12.004>.
- [30] T. Hu, J. Guilleminot, J.E. Dolbow, A phase-field model of fracture with frictionless contact and random fracture properties: Application to thin-film fracture and soil desiccation, *Comput. Methods Appl. Mech. Engrg.* 368 (2020) 113106, <http://dx.doi.org/10.1016/j.cma.2020.113106>.
- [31] H.M. Hilber, T.J.R. Hughes, R.L. Taylor, Improved numerical dissipation for time integration algorithms in structural dynamics, *Earthq. Eng. Struct. Dyn.* 5 (3) (1977) 283–292, <http://dx.doi.org/10.1002/eqe.4290050306>.
- [32] T. Hu, RACCOON, 2022, URL <https://github.com/hugary1995/raccoon>.
- [33] C.J. Permann, D.R. Gaston, D. Andrš, R.W. Carlsen, F. Kong, A.D. Lindsay, J.M. Miller, J.W. Peterson, A.E. Slaughter, R.H. Stogner, R.C. Martineau, MOOSE: Enabling massively parallel multiphysics simulation, *SoftwareX* 11 (2020) 100430, <http://dx.doi.org/10.1016/j.softx.2020.100430>.
- [34] S.J. Benson, T.S. Munson, Flexible complementarity solvers for large-scale applications, *Optim. Methods Softw.* 21 (1) (2006) 155–168, <http://dx.doi.org/10.1080/1055678050065382>.
- [35] T. Heister, M.F. Wheeler, T. Wick, A primal-dual active set method and predictor-corrector mesh adaptivity for computing fracture propagation using a phase-field approach, *Comput. Methods Appl. Mech. Engrg.* 290 (2015) 466–495, <http://dx.doi.org/10.1016/j.cma.2015.03.009>.
- [36] E. de Souza Neto, F.M.A. Pires, D.R.J. Owen, F-bar-based linear triangles and tetrahedra for finite strain analysis of nearly incompressible solids. Part I: Formulation and benchmarking, *Internat. J. Numer. Methods Engrg.* 62 (3) (2005) 353–383, <http://dx.doi.org/10.1002/nme.1187>.
- [37] R.C. Batra, R.R. Gummalla, Effect of material and geometric parameters on deformations near the notch-tip of a dynamically loaded prenotched plate, *Int. J. Fract.* 101 (2000) 99–140, <http://dx.doi.org/10.1023/A:1007504431357>.
- [38] B. Dodd, Y. Bai, Width of adiabatic shear bands formed under combined stresses, *Mater. Sci. Eng.* 5 (6) (1989) 557–559, <http://dx.doi.org/10.1179/mst.1989.5.6.557>.
- [39] R.J. Clifton, Response of materials under dynamic loading, *Int. J. Solids Struct.* 37 (1–2) (2000) 105–113, [http://dx.doi.org/10.1016/S0020-7683\(99\)00082-7](http://dx.doi.org/10.1016/S0020-7683(99)00082-7).
- [40] J. Johansson, C. Persson, H. Lai, M. Hörnqvist Colliander, Microstructural examination of shear localisation during high strain rate deformation of Alloy 718, *Mater. Sci. Eng. A* 662 (2016) 363–372, <http://dx.doi.org/10.1016/j.msea.2016.03.080>.
- [41] S. Li, W.K. Liu, A.J. Rosakis, T. Belytschko, W. Hao, Mesh-free Galerkin simulations of dynamic shear band propagation and failure mode transition, *Int. J. Solids Struct.* 39 (5) (2002) 1213–1240, [http://dx.doi.org/10.1016/S0020-7683\(01\)00188-3](http://dx.doi.org/10.1016/S0020-7683(01)00188-3).
- [42] T.J. Holmquist, Strength and Fracture Characteristics of HY-80, HY-100, and HY-130 Steels Subjected to Various Strains, Strain Rates, Temperatures, and Pressures: Tech. Rep., Defense Technical Information Center, Fort Belvoir, VA, 1987, <http://dx.doi.org/10.21236/ADA233061>.
- [43] B. Dodd, Y. Bai, Adiabatic Shear Localization, Frontiers and Advances Elsevier, 2012, <http://dx.doi.org/10.1016/B978-0-08-097781-2.00011-3>.
- [44] J. Lloyd, P. Jannotti, T. Jones, An overview of penetration behavior in magnesium alloys, *Mech. Mater.* 162 (2021) 104038, <http://dx.doi.org/10.1016/j.mechmat.2021.104038>.

- [45] A. Mota, W. Sun, J.T. Ostien, J.W. Foulk, K.N. Long, Lie-group interpolation and variational recovery for internal variables, *Comput. Mech.* 52 (2013) 1281–1299.
- [46] J. Duffy, Y. Chi, On the measurement of local strain and temperature during the formation of adiabatic shear bands, *Mater. Sci. Eng. A* 157 (2) (1992) 195–210, [http://dx.doi.org/10.1016/0921-5093\(92\)90026-W](http://dx.doi.org/10.1016/0921-5093(92)90026-W).
- [47] R.C. Batra, X. Zhang, On the propagation of a shear band in a steel tube, *J. Eng. Mater. Technol.* 116 (2) (1994) 155–161, <http://dx.doi.org/10.1115/1.2904266>.
- [48] R.C. Batra, B.M. Love, Crack propagation due to brittle and ductile failures in microporous thermoelastoviscoplastic functionally graded materials, *Eng. Fract. Mech.* 72 (2005) 1954–1979.
- [49] H. Wu, X. Zhuang, Z. Zhao, Extended GTN model for predicting ductile fracture under a broad range of stress states, *Int. J. Solids Struct.* 239–240 (2022) 111452.
- [50] R.C. Batra, X.S. Jin, Analysis of dynamic shear bands in porous thermally softening viscoplastic materials, *Arch. Mech.* 46 (1–2) (1994) 13–36.
- [51] R.C. Batra, K.I. Ko, An adaptive mesh refinement technique for the analysis of shear bands in plane strain compression of a thermoviscoplastic solid, *Comput. Mech.* 10 (6) (1992) 369–379, <http://dx.doi.org/10.1007/BF00363993>.
- [52] A. Kumar, B. Bourdin, G.A. Francfort, O. Lopez-Pamies, Revisiting nucleation in the phase-field approach to brittle fracture, *J. Mech. Phys. Solids* 142 (2020) 104027, <http://dx.doi.org/10.1016/j.jmps.2020.104027>.
- [53] C.J. Larsen, J.E. Dolbow, O. Lopez-Pamies, A variational formulation of Griffith phase-field fracture with material strength, *Int. J. Fract.* (2024) 1–9.